SIMULATIONS OF CERN TO PYHÄSALMI NEUTRINO EXPERIMENTS WITH GLOBES

Master's Thesis

Sampsa Vihonen

University of Jyväskylä
Department of Physics

Supervisor: Jukka Maalampi

Abstract

The research of long baseline neutrino oscillations is about to enter a new era. Years of studying data collected from reactor, atmospheric, solar, supernova and even some long baseline accelerator experiments have provided lots of new understanding and insight on neutrino oscillation mechanisms that follow from the standard three neutrino model. During this time most of the parameters that guide the neutrino flight have been measured to good precision, but a whole new kind of technology is needed to determine the ones that still remain unknown, such as the questions of mass ordering and the CP violation phase. The following years are expected to bring a new experiment generation to daylight to provide tools for solving these questions - neutrino superbeams that will be able to take beam energies to GeV scale.

The European response to the growing need for new experiment facilities lies in the LAGUNA-LBNO design study which has proposed a total of three next generation detector plans for measuring neutrino parameters among other things. This thesis explores the capabilities of two of these, LENA and GLACIER facilities, which are found suitable for the 2288-km-long CERN-to-Pyhäsalmi baseline. A simulation study is conducted to analyse the expected performance in these long baseline neutrino experiments for which the Pyhäsalmi mine is ranked as favoured site. The analysis is done with the general long baseline experiment simulator, GLoBES, using the latest results on the neutrino oscillation parameters.

We use the GLoBES software in this study to reveal the full potential of the proposed liquid scintillator (LENA) and liquid argon technology (GLACIER) for the case the facilities are placed in the Pyhäsalmi mine. Using a range of simulation methods available to GLoBES, we create a variety of demonstrations to evaluate the performance that would be expected to come from future experiment runs. Our approach presents a straightforward overview on applying the GLoBES package in a single experiment analysis using the CERN to Pyhäsalmi beamline as an example. Moreover, we attempt to take the study to higher precision using the most recent information available.

Contents

1 Introduction

Recent years have shown significant progress in experimental neutrino physics and particularly in the study of neutrino oscillations [1, 2, 3]. Years of data collection in various oscillation experiments has provided sufficient information to determine most of the oscillation parameters to good precision [4], and new plans have been announced to uncover those that still remain unknown [5]. One of the key developments in recent global parameter analysis has been the reactor neutrino data successfully ruling out the possibility of zero θ_{13} at a confidence level greater than $5\,\sigma$. Moreover, the parameter has been found to be $\sin^2 2\theta_{13} \approx 0.1$ according to the information gathered from Daya Bay [6] and RENO [7] reactor experiments and previous Double Chooz [8, 9], MINOS [10] and T2K data [11].

Finding the smallest mixing angle θ_{13} non-zero is an important landmark as it allows the possibility to study CP violation. This means that one may finally begin to investigate the elusive CP violation phase δ_{CP}, which is the last of the oscillation parameters in the Pontecorvo-Maki-Nakagawa-Sakata matrix that have remained unknown to this day. Future neutrino oscillation experiments will start to look for this parameter and it is hoped to bring better understanding over the alleged CP violation phenomenon in the leptonic sector. An accurate measurement is not possible, however, before the mass hierarchy question, i.e. the sign of Δm^2_{31}, is successfully answered. In order to solve these two degeneracy problems new experiment technologies and solutions such as magic baselines are being considered for long baseline experiments. In this thesis we look into one of these proposed neutrino experiments and explore its potential with numerical methods using the GLoBES package [12, 13].

The state of the parameters has similarly got significant progress in precision measurement with a recent paper narrowing the θ_{13} estimate down to $0.0214 < \sin^2\theta_{13} < 0.0279$ at 1σ confidence level. The other best-fit values are the following: The solar parameters are $\sin^2\theta_{12} = 0.312 \pm 0.016$ and $\Delta m^2_{21} = (7.65 \pm 0.02) \times 10^{-5}\,\mathrm{eV}^2$ as measured in KamLAND [14], whereas the atmospheric data from Super-Kamiokande has given $\sin^2\theta_{23} = 0.51 \pm 0.06$ [15]. Even the large squared mass difference Δm^2_{31} has been measured, and experiments have located its value to $(2.45 \pm 0.09) \times 10^{-3}\,\mathrm{eV}^2$ (normal mass hierarchy) and $(-2.34 \pm 0.09) \times 10^{-3}\,\mathrm{eV}^2$ (inverted mass hierarchy) [16]. The accurate determinations are perturbed by parameter degeneracies, among which most notable are the mass hierarchy, that is, the sign of Δm^2_{31}, and the intrinsic $\sin^2 2\theta_{13} - \delta_{\mathrm{CP}}$ degeneracy.

Measuring the unknown oscillation parameters in the PMNS matrix has been an actively studied field, and the extensive search has given rise to some future

large scale projects like NOνA [17] and LBNE [18] in the U.S. and T2HK [19] in Japan. The LAGUNA-LBNO [20, 21] has proposed three distinctive detector projects of which the ones based on liquid scintillator and liquid argon time projection chamber technologies, LENA [22] and GLACIER [23], are found to have the best potential as far detectors of the planned very long baseline experiment. The experiments could be started with a so called conventional beam with power of 0.7 MW, but later on a more intensive beam produced using HP-PS2 facility is planned to be used [24]. The CN2PY beamline planned is to maintain a multi-GeV scale neutrino beam for the nearly 2300-km-long baseline from CERN to the Pyhäsalmi mine. The length is remarkably close to the so called magic baseline, which would grant a significant advantage in mass hierarchy tests [25].

We exercise GLoBES to probe the potential of these facilities to study the fundamental neutrino oscillation parameters in presence of parameter degeneracies and focus on examining their ability to provide a clean measurement on $\mathtt{sgn}\left[\Delta m^2_{31}\right]$. In addition to mass hierarchy, we also study sensitivity on detecting CP violation and the precise value of θ_{23}. We also test the experiment's ability to yield information on the true value of δ_{CP}.

The thesis is organized as follows. Whereas the rest of Ch. 1 explain the standard physics of neutrino oscillations in the three-flavour case, the scrutinized detector systems and neutrino beam is revisited in Ch. 2. The LAGUNA facilities are then studied in detail in Ch. 3 as we begin to describe the experiment setups for LENA and GLACIER and think how one could simulate them. The overall GLoBES analysis and simulation methods are examined in Ch. 4, where all the details concerning the event rate and χ^2 calculation is discussed. The simulation specifics are outlined in Ch. 5 and the data analysis in Ch. 6, where the simulation process is explained step by step. The work is summed up in Ch. 7 with a throughout analysis on the collected results.

1.1 Introductory oscillation physics

Neutrinos are found to oscillate on flight by transforming from one flavour state to another. In vacuum this oscillation process is governed by the Pontecorvo-Maki-Nagakawa-Sakata matrix (PMNS) which is parametrized as follows [1]:

$$U = \begin{pmatrix} 1 & 0 & 0 \\ 0 & c_{23} & s_{23} \\ 0 & -s_{23} & c_{23} \end{pmatrix} \begin{pmatrix} c_{13} & 0 & s_{13}e^{-i\delta_{CP}} \\ 0 & 1 & 0 \\ -s_{13}e^{i\delta_{CP}} & 0 & c_{13} \end{pmatrix} \begin{pmatrix} c_{12} & s_{12} & 0 \\ -s_{12} & c_{12} & 0 \\ 0 & 0 & 1 \end{pmatrix}. \quad (1)$$

We have denoted $c_{ij} = \cos\theta_{ij}$ and $s_{ij} = \sin\theta_{ij}$, where θ_{ij}, $i, j = 1, 2, 3$, are the

so called mixing angles and δ_{CP} is a phase factor that describes the effect of possible CP violation.

The probability of a neutrino of flavour l to transform into flavour l' at energy E and traversed length L is given by the following formula [25]:

$$P_{ll'}(E) = \delta_{ll'} - \sum_{i,j\,;\,i>j} \left[4 \sin^2 \Delta_{ji}\ \mathfrak{Re}\, W^{ij}_{ll'} - 2 \sin 2\Delta_{ji}\ \mathfrak{Im}\, W^{ij}_{ll'} \right], \qquad (2)$$

$$\Delta_{kj} = L\, \Delta m^2_{jk}/4E, \;\; W^{jk}_{ll'} = U^*_{lj}\, U_{l'j}\, U_{lk}\, U^*_{l'k}$$

for mixing matrix U.

The so called neutrino parameters, which the design study is set to search, comprise of Δ_{kj} and U, which are given in mixing angles θ_{ij}, phase factor δ_{CP} and the so called squared mass difference $\Delta m^2_{ij} = m^2_i - m^2_j$. In the standard three neutrino model the mixing matrix U is parametrized with the PMNS matrix (1).

The most general form of the mixing matrix U contains also two so-called Majorana phases, which can be implemented by multiplying U in Eq. (1) with the diagonal matrix $diag(1,\, e^{i\,\alpha},\, e^{i\,\beta})$. These two phases do not affect the oscillation probabilities (2), however, so we will not include them into our calculations.

1.2 Experimental search for oscillation parameters

One of the goals of neutrino oscillation research is to measure the neutrino parameters appearing in the transition probability formula as precisely as possible. This task is demanding due to the complex structure of the probability formula, which suffers from parameter degeneracies and correlations. On the other hand, the measurement process is also affected by the limits of the measuring technology. A clean measurement often requires special conditions, which is why it is important to understand the nature of both theoretical and technical limits before building a real experiment facility [4].

Neutrino experiments are rarely able to access oscillation parameters directly. The θ_{13} parameter, for example, is often determined by measuring $\sin^2 2\theta_{13}$ due to the structure of the probability formula. Furthermore the large squared mass difference is determined at accelerator experiments by observing the mass term in the muon disappearance channel [16]:

$$\Delta m^2_{\mu\mu} = \Delta m^2_{31} - (\cos^2 \theta_{12} - \cos \delta_{\mathrm{CP}}\ \sin^2 \theta_{13}\ \sin 2\theta_{12}\ \tan \theta_{23})\, \Delta m^2_{21}. \qquad (3)$$

The measured quantity shown in Eq. (3) is dominated by Δm^2_{31}, but an accurate measurement would require further knowledge on other parameters as well. The mass term $\Delta m^2_{\mu\mu}$ serves as a good approximation of Δm^2_{31}, but the process leads to different solutions for different mass hierarchies. Similar difficulties apply to measurements of other parameters too. It is the main challenge of neutrino experiments to overcome these problems.

Most superbeam experiments are designed to study oscillated neutrinos muon neutrino beams which become subject to matter effects when traversing the Earth's core on their way to distant detectors. In such case the transition probability can be approximated from Eq. (2) as [25, 26]

$$\begin{aligned} P(\nu_\mu \to \nu_e) \cong\ & \sin^2 2\theta_{13}\, \sin^2\theta_{23}\, \frac{\sin^2[(1-\hat{A})\Delta]}{(1-\hat{A})^2} \\ & - \alpha \sin 2\theta_{13}\, \xi\, \sin\delta_{\mathrm{CP}}\, \sin(\Delta)\, \frac{\sin(\hat{A}\Delta)}{\hat{A}}\, \frac{\sin[(1-\hat{A})\Delta]}{1-\hat{A}} \\ & + \alpha \sin 2\theta_{13}\, \xi\, \cos\delta_{\mathrm{CP}}\, \cos(\Delta)\, \frac{\sin(\hat{A}\Delta)}{\hat{A}}\, \frac{\sin[(1-\hat{A})\Delta]}{1-\hat{A}} \\ & + \alpha^2 \cos^2\theta_{23}\, \sin^2 2\theta_{12}\, \frac{\sin^2(\hat{A}\Delta)}{\hat{A}^2} + \mathcal{O}(\alpha^3), \end{aligned} \tag{4}$$

where $\hat{A} := \pm(2\sqrt{2}G_F\, N_e\, E)/\Delta m^2_{31}$, $\xi := \cos\theta_{13} \sin 2\theta_{12} \sin 2\theta_{23}$, and $\Delta := \Delta_{31}$. Constants G_F and N_e denote the Fermi constant and number of electrons per volume in the medium the neutrinos are traversing. The expression follows from expanding Eq. (2) in powers of $\alpha := \Delta m^2_{31}/\Delta m^2_{21}$ and θ_{13}.

The structure of the probability formula in Eq. (4) allows to separate the δ_{CP} containing terms from others in the following way. Depending on the research objectives of the neutrino experiment, i.e. what parameter is wanted to measure, $\hat{A}$ and Δ can be modified by choosing beam energy and baseline length conveniently. The mass hierarchy sensitivity, for instance, can be optimized by choosing Δ and $\hat{A}$ so that the δ_{CP} containing terms are suppressed in Eq. (4). In such case the $\sin^2 2\theta_{13}$ containing term would dominate with a small background coming from the higher order terms where $\alpha \geq 2$. Such conditions are known as the so called magic baselines [25] and their associated energies.

1.3 Simulating experiments with GLoBES

The software we are using in this paper to perform the simulations is known as the General Long Baseline Experiment Simulator i.e. GLoBES [27]. GLoBES

is a modern open source software package, which includes relatively straightforward computation tools for $\Delta\chi^2$ computing. It also provides a simple way to describe experiment settings on abstract level with a text format and offers a number of C functions to compute many low-level features such as event rates and oscillation probabilities. The simulator approximates neutrino experiments with quick computation algorithms, which provide a good preliminary evaluation model to estimate experiment performance. Today GLoBES is used in most simulation studies that concern long baseline neutrino oscillation experiments.

GLoBES has several built-in algorithms to compute the final event rates that take into account neutrino propagation and energy-dependent efficiencies. In this thesis we present a sample computation method that yields final event rates by sorting events into equidistant energy bins via numerical integration. This method gives the number of successfully reconstructed neutrino events representing a given transition channel (c) and energy bin (i) with the following formula [12, 13]:

$$n_i^c = \frac{N}{L^2} \sum_j \Phi(E_j) P_{ll'}(E_j) \sigma(E_j) K_i(E_j) \Delta E_j, \tag{5}$$

where j labels the neutrino energy bins, N is the normalization factor, L baseline length, and Φ, $P_{ll'}$, σ and K_i represent the flux, transition probability, cross section and energy resolution terms, respectively. The energy bin width ΔE_j is associated to the bin that corresponds to neutrino energy E_j. The event rate formula in Eq. (5) is a rather simplistic example of the computation methods used by GLoBES, but it gives for practical purposes a sufficiently good estimate in straightforward processes such as neutrino propagation in superbeam experiments.

With necessary accelerator, baseline and detection information specified in an AEDL file by the user, the system uses a special algorithm to compute event numbers for simulated experiment. The GLoBES software is then able to calculate various properties by extracting the information it gets from simulated event numbers. These techniques depend much on the nature of the task, and they are discussed in greater detail in Ch. 4. The construction of an AEDL file also requires good understanding over the different information elements concerning the experiment and how they are combined, which is detailed in Ch. 5.

In this study we are interested in using the $\Delta\chi^2$ analysis tool to find out the values of $\sin^2 2\theta_{13}$ and δ_{CP} for which the simulated neutrino experiments would

be able to determine the correct mass hierarchy and detect CP violation in the future. The simulator estimates the event rates that can be expected to be detected at the future neutrino experiments and compares the impact of the different oscillation parameters in the light of that data. We examine the ability to identify mass hierarchy, probe CP violation and test $\sin^2 2\theta_{13} - \delta_{CP}$ and (θ_{23},90°- θ_{23}) degeneracies in a set of neutrino experiments with the simulated data. We study the ability of LENA and GLACIER detectors to rule out the wrong solution in each case when targeted with an intense HP-PS2 muon neutrino beam from CERN, going through all possible alternatives with the unknown oscillation parameters. The overall data analysis is carried out in Ch. 6.

2 Long baseline experiment scenarios

The recent LAGUNA-LBNO design study features three different detector systems, which are designed to study various phenomena in neutrino physics and proton decay, using both man-made neutrino beams and neutrinos originating from astrophysical sources. When operational, these three detectors will represent state-of-art engineering in water Cherenkov (MEMPHYS), liquid scintillator (LENA) and liquid argon (GLACIER) technologies. In this section the potential and the basics of the such neutrino detector technologies are described as part of a long baseline oscillation program. Also different beam and baseline alternatives are examined, showing how these contribute to experimental neutrino research.

2.1 Superbeams and baselines

The most prominent long baseline neutrino oscillation experiments are based on multi-GeV powered superbeams. It represents a feasible and powerful experiment type that is capable of solving the degeneracy problems that hinder precise measurements at present ongoing experiments [28, 29]. Superbeams are based on upgraded conventional neutrino beams, which maintain continuous neutrino creation by accelerating protons to high energies. Energetic beams are particularly useful at long baselines where matter effects become significant. Shorter baselines, on the other hand, benefit from better statistics and lesser degeneracy impact. The beam composition is also analysed with a second detector that is placed at a short distance from the beam source, known as the near detector. In this thesis, however, we simulate the neutrino experiments with only far detectors taken into account.

There are several major advantages in long baseline superbeam experiments compared with those using shorter baselines. Longer baselines make the transition probabilities peak at higher energies that in turn improves cross sections [30]. Both of these factors increase statistics in the planned experiment, leading to better sensitivities. Furthermore, the enhanced matter effects increases the difference caused by different mass hierarchy solutions in detected event rates, and thus improves the ability to exclude the wrong mass hierarchy solution at different values of θ_{13} and δ_{CP}. A special case is reached at the so called magic baselines and energies, at which the δ_{CP} influenced terms totally vanish at the probability formula in Eq. (4). With standard assumptions 2450 km is one of such magic lengths [25].

Whereas very long baselines are ideal for probing the mass hierarchy, the vanishing δ_{CP} terms make the magic lengths disfavouring for searching CP violation. Some papers [30] show that the matter effects decrease sensitivity for the CP violation as the role of the parameter degeneracies becomes significant in addition to lower matter effects. Shorter baselines also involve often better statistics due to the lesser spreading of the beam, and the peak energies become lower and therefore easier to reach at shorter distances. Moreover, evidence has been pointed out that the degenerate mass hierarchy solution could result in erroneous misinterpretation of experiment data if the true hierarchy is not known [31]. This supports the strategy that the mass hierarchy is first studied at a baseline close to magic a length and a shorter baseline is then used to study the CP violation. The baseline between CERN and Pyhäsalmi sites would provide very good mass hierarchy detection conditions with its 2288-km-long baseline (see e.g. [32]).

2.2 Liquid scintillators

Liquid scintillating technique is a detection method where organic compounds are used to interact with incoming neutrinos (see e.g. [22]). The compound molecules excited by interaction emits scintillation light which is detected by photomultiplying tubes (PMT) placed to surround the detector fluid. Liquid scintillators have a very low energy threshold coupled with a good energy resolution and background discrimination ability, which makes this detection method very suitable for probing low energy phenomena. The detector type is also found very promising for detecting GeV-scale neutrinos, and thus it could also act as a far detector in a long baseline experiment. Examples of neutrino detectors advocating liquid scintillating technique include the Borexino detector in Italy [33] and KamLAND in Japan. Also the soon launching NOνA experiment utilizes liquid scintillating method in its far detector.

The detector vessels are typically filled with mineral oil that composes of aromatic hydrocarbons. The incoming neutrinos interact with the free valence electrons in benzene rings prompting them to exited states. The light emitted from discharging excitation states is then identified at the PMT's allowing the system to count the events. Also charged particles passing through the scintillator fluid are observable through their ionization tracks, providing further information to later reconstruct the energy and flavour of incident neutrinos [27]. The detector fluid is protected from unwanted (e.g. atmospheric and solar) neutrinos with a water cover.

When liquid scintillators are realized in large scales, where active detector masses may reach multi-kiloton weights, the emission spectra of the organic compounds is usually not sufficient to produce observable events. In order to avoid information loss, at least one solute is added to the scintillator solvent to shift the emission wavelength to a higher region where scintillation can be observed. Information of the occurring events can then be extracted from the analysis of the scintillation light [25].

Liquid scintillators observe neutrinos from two distinct reaction types: elastic collisions through charged and neutral current events and inverse beta decay. Elastic collisions are the most numerous processes, in which neutrinos scatter from electrons or the atomic nuclei in the scintillator liquid, $\nu + e^- \rightarrow \nu + e^-$. This process has a marginal energy threshold and it allows observation of neutrinos with low energy.

Neutrinos captured in inverse beta decay, on the other hand, emit a positron and neutron which eventually turn into photons as the positron annihilates with another electron and neutrino is recaptured with a delay:

$$\bar{\nu}_e + p \rightarrow \bar{\nu}_e + n \tag{6}$$

This process comes with a distinguishable signature and a threshold energy of approximately 1.8 MeV, which is low in multi-GeV scale. Whereas neutrinos are detected through elastic collisions, electron antineutrinos are effectively identified with the inverse beta decay. The energy threshold information defines the energy resolution in the overall detector performance and it is a valuable tool for background discrimination. The minimum energy for detecting electron scattering is even lower, giving liquid scintillation technique high energy resolution and good background discrimination capability.

Liquid scintillators have been shown in various Monte Carlo studies to be quite promising for detecting neutrinos in long baseline oscillation experi-

ments. Examples of possible future experiments where liquid scintillator detectors have been considered as a possible detector solution include SNO+ (next phase to Sudbury Neutrino Observatory) in Canada [34], INO (Indian-based Neutrino Observatory) in India [35] and LAGUNA-hosted LENA (Low Energy Neutrino Astronomy) in Europe.

2.3 Liquid argon time projection chambers

Over the years liquid argon based detecting techniques have gained interest through significant development it provides in identifying neutrino energy, trajectory and type with high-purity liquid-form argon (see e.g. [23]). Liquid argon detects neutrinos through the following reaction:

$$^{40}\mathrm{Ar} + \nu \rightarrow {}^{40}\mathrm{K} + e^{-}, \tag{7}$$

where a neutrino of any flavour is absorbed into an argon nucleus via a reaction similar to inverse beta decay. One of the advantages in liquid argon medium is that it is capable of tracking the charged particles it emits as a result of interacting with neutrinos. The technique allows precise charge identification and estimation of the time neutrino event occurs. Liquid argon benefits from fairly inexpensive production costs and homogeneous form that simplifies the detection process as composed with that of liquid scintillators. The liquid is also fully active, meaning that it is far more efficient with respect to volume in comparison with e.g. water Cherenkov detectors.

An example of current technology using liquid argon in neutrino detectors is the so called liquid argon time projection chamber [36], which combines the prospects of bubble chamber and scintillator technique. The chamber is coupled with an electric field, which causes the ionized charges to drift towards the detector's wall where it is picked up by sensors. The scintillation light from argon nuclei can also be used to advantage as it allows to estimate the time at which neutrino events occur.

Liquid argon time projection chambers features remarkable performance which has inspired many large scale experiment proposals. The technology has been previously tested in neutrino experiments like ICARUS (Imaging Cosmic And Rare Underground Signals) in Italy [37] and ArgoNeuT (Argon Neutrino Teststand) in the USA [38]. Since the future prospects have been proved remarkable in many simulation studies, large scale liquid argon time projection chambers have been proposed in many design studies, including LBNE (Long Baseline Neutrino Experiment) in the U.S. and LAGUNA-LBNO's GLACIER (Giant Liquid Argon Charge Imaging ExpeRiment) in Europe.

2.4 Water Cherenkov detectors

When a charged particle traverses in water at speed higher than the speed of light, the so called Cherenkov radiation is emitted. Cherenkov radiation is the optical equivalent to sonic boom taking place as a result of exceeding the speed of sound in air. This phenomenon is the foundation behind a whole detector class, known as water Cherenkov detectors. This radiation is observed at photosensors typically attached to detector's wall.

The advantages of the water Cherenkov technology are its reliability and the cheap production cost of its water content as compared with liquid scintillator and liquid argon mediums. Water Cherenkov detectors are currently the only detector type for which it is feasible to build very large detector chambers. The detector technology has sufficient resolution to measure energy, position and arriving angle of particles it detects with decent accuracy. A well known example of water Cherenkov detectors is Super-Kamiokande, which has been operating in Japan since 1996. The technology is well proven, though its capabilities are somewhat limited with respect to the liquid scintillator and argon options - a water Cherenkov detector typically needs to be built several times larger to reach comparable sensitivities. Therefore this detector type is suitable for systems where resolution does not need to be so high and the well understood topology can be used to advantage. The detector type is only capable of studying sub-GeV energies to maintain sufficient accuracy, which limits its use to shorter baselines.

Among the planned future neutrino oscillation experiments, where water Cherenkov detector is being considered, as examples are the next phase of the Super-Kamiokande experiment in Japan, the Hyper-Kamiokande, UNO in the U.S. (Underground Nucleon decay and Neutrino Observatory) [39] and MEMPHYS in Europe (MEgaton Mass PHYSics) [40]. Despite its obvious importance, we are not going to include the water Cherenkov detector option within the framework of this study as it is not suitable for the Pyhäsalmi detector site, as shown by numerical studies [30, 42].

3 The experiment setup

The aim of the future long baseline neutrino oscillation experiments is to solve the mass hierarchy problem and probe the CP violation among neutrinos. The LAGUNA collaboration has proposed the liquid scintillator detector LENA and liquid argon time projection chamber GLACIER. For the liquid scintillator and liquid argon projects, the considered detector site has been proposed to

establish at the Pyhäsalmi mine in Finland. In this chapter we look into these two detector setups and quantify the distinctive properties that describe their behaviour assuming the planned HP-PS2 synchrotron facility at CERN as the beam source in each case.

3.1 The CN2PY beam

Within the framework of the LAGUNA-LBNO project, the CERN-based working group started to study the feasibility of upgrading the SPS facility (Super Proton Synchrotron) to technology that could successfully provide an intense neutrino beam by accelerating protons to high energies. The design study discusses a multi-step approach aiming to equip SPS technology to reach intensities that were available at the CNGS beam [43]. If successful, the upgraded neutrino beam will provide muon neutrinos at multi-GeV energies that allows to scan neutrino energies with intensity about the first oscillation maximum, even for very long baselines.

The grand goal of such beam technology is to reach neutrino energies where oscillation probabilities following Eq. (2) reach their maximum and minimum points. The first oscillation maximum is typically sufficient to determine the mass hierarchy and probe the CP violation, but the second oscillation maximum could have use in improving sensitivity and studying non-standard interactions. The energies of the corresponding minimum and maximum points are associated with the baseline length, as seen in Eq. (4). In this paper we consider the baseline between CERN and the considered detector location at the Pyhäsalmi mine.

In the case of very long baseline distance, such as the one between CERN and Pyhäsalmi, the superbeam is planned to reach 50 GeV proton energy with 2.4 MW average power per operational year (typically 10^7 s per year). The corresponding yearly proton production would then be 3.0×10^{21} useful proton collisions on target (POT), which is approximately an order of magnitude greater than those of NOνA and T2K [44] beams. The resulting HP-PS2 beam is scheduled to run 2 years in neutrino mode and 8 years in antineutrino mode [42, 45] for baselines with 130 km and 5+5 years for longer distances. The antisymmetry of the run times comes from the smaller cross section of antineutrino interactions compared with the neutrino cross sections. This run setup is designed to yield comparable numbers of neutrino and antineutrino events.

The baseline we are focused on in this study is longest of the considered within the LAGUNA-LBNO project, asserting Pyhäsalmi as preferred detector site. Previous simulator studies [29, 30, 45], have shown this baseline length as ideal

one for mass hierarchy tests and respectively less effective for δ_{CP} measurements. The baseline would also house good potential for testing non-zero θ_{13} mixing angle which benefits from the higher beam energy.

3.2 The LENA detector

LENA (Low Energy Neutrino Astronomy) is a multi-purpose neutrino detector that uses liquid scintillation technology for observing neutrinos from natural and man-made sources. The proposed detector system is originally designed to detect neutrinos from the lower end of the energy spectrum, focusing mainly on sources of the likes of galactic core-collapse supernovae, nuclear reactions at the Earth's interior and the faint signals of diffuse supernova neutrinos. It has been also found suitable at GeV scale, where it is capable to observe nucleon decay if it occurs and act as far detector in a long baseline accelerator system. If approved, LENA will stand 100 meters tall with a diameter of 26 meters and cylindrical shape. The 50 kton target volume is surrounded with a muon veto and it will be buried deep underground to shield it from unnecessary cosmic ray background. The detector construction is illustrated in Fig. 1. As a liquid scintillator, LENA's technology is supported by the success of KamLAND and Borexino experiments. The advantage LENA has over KamLAND and Borexino is its superior size that is comparable to that of the Super-Kamiokande.

The active volume of LENA composes of liquid scintillator for which linear-alkyl-benzene (also known as LAB) solvent with a combination of 2,5-diphenyl-oxazole (PPO) and 1,4-bis-(o-methyl-styryl)-benzene (Bis-MSB) solutes are currently favoured. The detector study is still subject to active R&D process. The scintillator substance covers 43.2 kton of the total weight, and it has an energy resolution of 3% at energies below 10 MeV and approximately 5% at higher energies. As it was pointed out in Sec. 2.2, liquid scintillators have a 1.8 MeV energy threshold for detecting inverse beta decays and around 200 keV for observing electron scattering events, where the electron scattering limit comes from the small portion of the radioactive ^{14}C isotope in the scintillator liquid. Therefore LENA can be estimated to have the total energy resolution of approximately 5% with respect to the energy it measures [46]. Low energy resolution and good background discrimination ability lead LENA to high event statistics with respect to the flux of incoming neutrino stream.

Another important issue in neutrino detection capacity arises when the neutrino beam is taken into account. Superbeam fluxes will be optimized to reach best sensitivity at the energies of their first oscillation peak. A muon neutrino beam can be expected to be contaminated by a small muon antineutrino

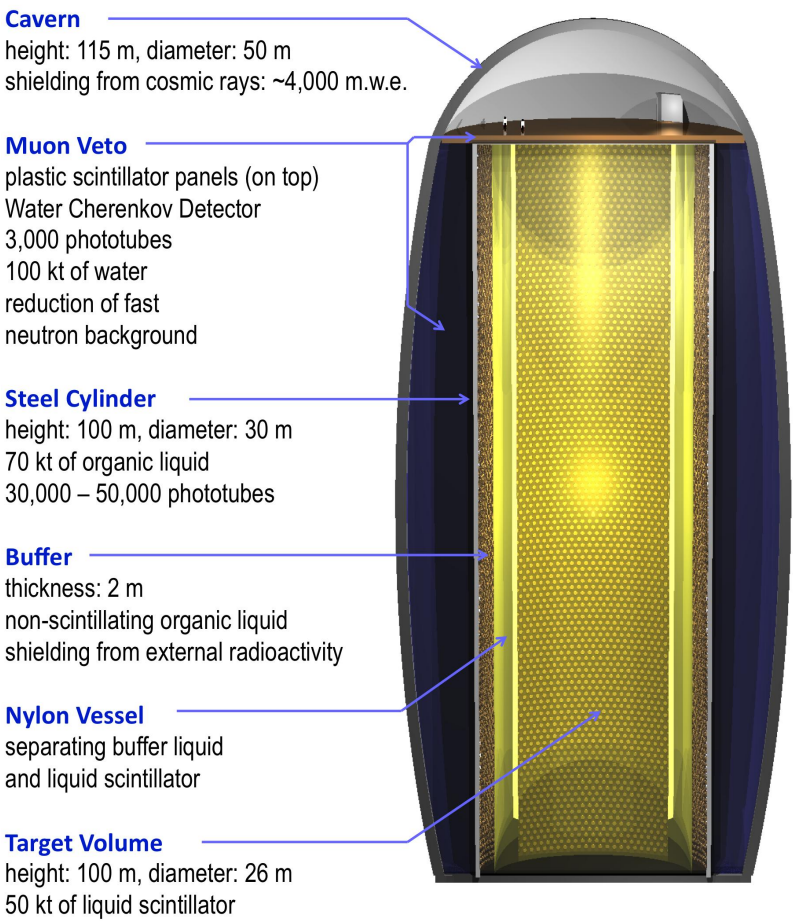

Figure 1: The schematical view of the LENA detector [22].

component, as well as components of electron neutrinos and antineutrinos. These contaminations are usually of a few percent order, but they need to be taken into account. Moreover, the beam background includes NC events added with the fraction of CC muon neutrino events that are mistaken as electron events. The NC compontent is dominant in observing muon neutrinos and the misidentified NC events can be rejected by approximately 90% chance in LENA, depending on the technological development at the time the detector construction is completed [42].

3.3 The GLACIER detector

The GLACIER (Giant Liquid Argon Charge Imaging ExpeRiment) will be running on liquid argon time projection chamber technology. The advantages of this technology is the superior event reconstruction ability with good NC rejec-

tion and neutrino detection efficiency. The detector composes of a large tank filled with liquid argon as illustrated in Fig. 2. The vessel has photosensing instrumentation attached to its walls, and there is an external electric field throughout the detector tank that points downwards. Negatively charged electrons created in the neutrino-argon interaction (cf. Eq. (7)) are hence drifted to the top of the vessel where charge identification electronics are placed.

GLACIER is expected to have nearly perfect detection capability for both muon and electron neutrinos and their antiparticles. The efficiency varies from 80% through 100% [42, 46] depending on energy, the average being roughly 90% for both neutrino classes. An overall of 20% energy resolution can be expected with respect to the reconstructed energy in muon neutrinos and antineutrinos. The percentage is 150 MeV for electron neutrinos and antineutrinos. The energy threshold to trigger the neutrino-argon interaction is estimated to be 0.5 GeV. It is important to note here that the instrumentation is under R&D, and these values are only guessed averages.

The liquid argon content is homogeneous and fully active, and detector masses as big as 100 kton are considered possible, which is also the proposed size of the GLACIER laboratory. The present level of expertise in the petrochemistry industry allows to produce high purity argon in liquid form very effectively. Nevertheless, a sufficient supply of liquid argon during the construction of GLACIER might be a critical issue. The cavern excavation will also be a challenge due to the large size of the detector. GLACIER will also have an option to upgrade to magnetic field through a detector extension, allowing options

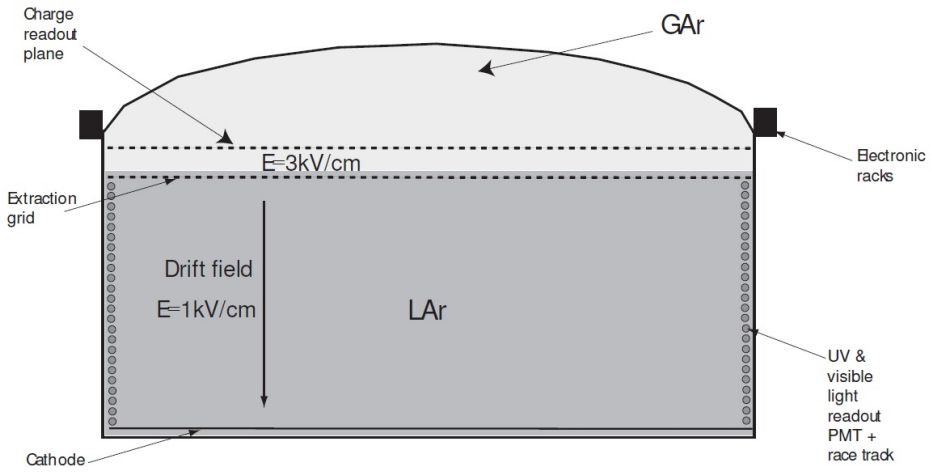

Figure 2: The schematic view of the GLACIER detector [47].

like charge discriminating and precise kinematics, which is beneficial if the detector one day is combined with a neutrino factory beam [41].

Most of the building challenges encountered will arise from extrapolating the scale of the detector to a new order of magnitude. Prospects of liquid argon time projection chambers have been studied in small prototype versions (e.g. ArgoNeuT had only 175 litres of argon) with promising results, but new problems might emerge when the size is taken to 100 kton. When completed, however, GLACIER is expected to provide unprecedented sensitivity according to simulation studies (see e.g. [30] and [42]).

4 Simulation methods

The simulation study is done using the GLoBES routines which are particularly suitable for the simulations of superbeam experiments and are convenient due to their rather simple topology. In this chapter we introduce the computing methods we use to calculate event rates and χ^2 distributions. A more general description of the GLoBES software can be found in [12, 13]. For more information on the methods, consult [27].

4.1 Event rate computation and integrated luminosity

GLoBES is a modular software that simulates neutrino beam as it travels from source to detector, where subsequent neutrino interactions with detector substance are detected with appropriate instrumentation. The simulator computes oscillation probabilities and corresponding event rates for the channels that are set for observation in the simulated experiment. The total event rate in prospective beam experiment is roughly proportional to the product of fiducial detector mass, experiment running time and beam power, i.e., we can write

$$\mathcal{L} \sim \text{Fiducial detector mass} \times \text{Running time} \times \begin{cases} \text{Source power} \\ \text{Useful parent decays} \end{cases} . \tag{8}$$

This quantity is called the integrated luminosity. It is a useful measure to estimate the performance of a single far detector experiment through the average event rate numbers the experiment would eventually produce if completed.

The fiducial detector mass appearing in Eq. (8) means the fraction of detector mass that is able to interact with incoming neutrinos. In liquid argon experiments the whole detector mass is active, but in liquid scintillator detectors this

applies to only part of the total mass. The fiducial detector mass is typically given in the units of kilotons for superbeam experiments and of tons for reactor experiments. The second term in Eq. (8) defines the running time of the experiment in years, the last term represents the source power, which relates to the number of created neutrinos. The source power can be also expressed as the number of useful POT collisions per year, often used for superbeam experiments.

The software calculates event rate vectors by implementing experiment descriptions, which are given in the so called glb-files. These files are written with Advanced Experiment Definition Language, AEDL, which allows an informative description of various kinds of oscillation experiments. The software calculates differential neutrino rates by running the data on glb-files through suitable computation algorithm. In neutrino factory experiments, for instance, the differential number of events per GeV is computed with

$$\begin{aligned} n = {} & 5.2 \times x \times E \times f \\ & \times \texttt{@norm} \times \texttt{@power} \times \texttt{@stored\_muons} \\ & \times \texttt{@time} \times \texttt{@target\_mass} \times \texttt{@baseline}^{-2}, \end{aligned} \tag{9}$$

where the @-marked parameters are elements of glb-files and presented in AEDL syntax. This corresponds to the differential event rates that do not account oscillation effects and to efficiencies related to the event detection and reconstruction process. Eq. (9) is an intermediate step in the event rate calculation process, where it is used to evaluate the event rate formula that GLoBES uses through efficiencies and smearing tools. In Eq. (9) terms $x \equiv \sigma/E$, E and f are defined as the differential cross section against energy, neutrino energy and flux of the neutrino beam, respectively. The overall constant 5.2 is an undocumented fudge factor that arises from the GLoBES software encoding. Integrated luminosity $\mathcal{L}$ given in Eq. (8) appears here as the product `@power` $\times$ `@time` $\times$ `@stored_muons`, which includes the associated beam power, running time and number of parenting muons. Similarly, the baseline and detector mass are accounted with the terms `@baseline` and `@target_mass`, respectively. These elements need to have matching units, and an overall normalization factor is therefore given in `@norm`. Eq. (9) is also applicable to superbeams in which case `@stored_muons` stores the number of useful POT collisions instead.

4.2 Chi-squared functions

The most sophisticated data analysis tool GLoBES provides is the χ^2 calculator which computes the χ^2 goodness-of-fit test for two different event rate sets. The χ^2 method is a widely adopted statistical test to find out how well two sets of event rates computed from different oscillation parameters fit together. The resulting χ^2 function gives the confidence level at which the tested oscillation parameter values can be ruled out with referenced data. GLoBES uses a standard algorithm to calculate χ^2 values numerically, taking into account parameter correlations as well as systematic errors.

In our simulation study we use the standard GLoBES functions assuming two sources of systematic errors, one related to signal events and the other to background events. The presence of systematics is demonstrated with the nuisance parameters $\zeta_1, \ldots, \zeta_k$ through the pull method, which imposes a small penalty on the χ^2 function for each systematic error. Using event rates obtained from i^{th} bin, the core χ^2 function is then

$$\chi^2(\omega, \omega_0, \zeta_1, \ldots, \zeta_k) = \sum_{i=1}^{n} 2\left(\tilde{T}_i - \tilde{O}_i\,(1 - \ln\frac{\tilde{T}_i}{\tilde{O}_i})\right) + \sum_{j=1}^{k} \zeta_j^2, \tag{10}$$

where the so called tested and observed rates (see below) are denoted with $\tilde{T}_i$ and $\tilde{O}_i$, ω represents the oscillation parameters and n gives the number of bins.

Test rates and observed rates are event rates that GLoBES calculates from the oscillation parameter sets that are considered for test and reference. Test rates are computed from an arbitrary set of parameter values with which one wants to test the performance of the simulated neutrino experiment. The observed rates, on the other hand, represent the data that correspond to the parameter values, which one ultimately believes to be closest to the truth. These are often called as true values, usually retrieved from best fit values of previous experiments. The χ^2 value therefore indicates the confidence level at which test values can be ruled out with true values. An example is in place; if a neutrino experiment is expected to yield N_i^{ex} signal events and N_i^{bg} background events in the i^{th} bin, the rate of observed events is given by

$$\tilde{O}_i = N_i^{\text{ex}}(\omega_0) + N_i^{\text{bg}}(\omega_0), \tag{11}$$

where ω_0 is the set of true values.

Test rates are computed in a similar manner but from the oscillation parameter set that is considered for testing. They are affected by systematics, which

cause a shift in computed event rates. In this study we implement a standard GLoBES systematics function, which calculates the test rates with

$$\tilde{T}_i = N_i^{\mathrm{ex}}(\omega)\,[1+\pi^a\zeta_a] + N_i^{\mathrm{bg}}(\omega)\,[1+\pi^b\zeta_b], \tag{12}$$

which uses ω as the set of test values. The magnitude of each error is given by constants π^a and π^b. They are usually of the order of few percents. Eq. (12) represents a typical situation where energy normalization causes systematic uncertainty.

The use of the test and observed rates allows the simulator to test arbitrary sets of oscillation parameter values against data computed from parameter values that one considers true ones. The χ^2 computation algorithm estimates the event rates that would come out with these two parameter value sets and compares their compatibility with Poissonian functions. In Eq. (11) and (12) we refer to the test values as ω and the true values as ω_0.

GLoBES has also a more sophisticated systematics function which becomes useful when there is a systematic error in energy calibration. In such case the test rate formula given in Eq. (12) becomes

$$\begin{aligned}\tilde{T}_i = {} & (1+\pi^c\zeta^c)\left[(1+\pi^a\zeta^a)\,[N_{i+1}^{\mathrm{ex}} - N_i^{\mathrm{ex}}](\delta_c - k) + (1+\pi^a\zeta^a)\,N_k^{\mathrm{ex}}\right] \\ & + (1+\pi^d\zeta^d)\left[(1+\pi^b\zeta^b)\,[N_{i+1}^{\mathrm{bg}} - N_i^{\mathrm{bg}}](\delta_d - k) + (1+\pi^a\zeta^a)\,N_k^{\mathrm{bg}}\right],\end{aligned} \tag{13}$$

where $\delta_x = \zeta_x\,(i + {E'}_{\mathrm{min}}/\Delta E + 1/2) + i$ and k is the integer part of δ_x, x=c,d. Here ζ_c and ζ_d are two new nuisance parameters which are set to describe the energy calibration with coefficients π_c and π_d. The calibration error is accounted by replacing computed event rates in each bin to correspond to the new normalized energy. The energy values are calculated with linear interpolation from the smallest reconstructed energy E'_{min} and bin width ΔE.

The full χ^2 distribution is computed by minimizing the χ^2 function over all nuisance parameters, so the core part of the general formula for χ^2 values reads as follows:

$$\chi^2_{\mathrm{pull}}(\omega,\omega_0) = \min_{\zeta_i}\left[\chi^2(\omega,\omega_0,\zeta_1,\ldots,\zeta_k) + \sum_{j=1}^{k}\frac{\zeta_j^2}{\sigma_{\zeta_j}^2}\right]. \tag{14}$$

The χ^2 computation algorithm determines the test rates given in Eq. (12) or Eq. (13) and the observed rates from Eq. (11), and computes then the values of the

core χ^2 function with Eq. (10). The effect of systematics is taken into account through minimizing over nuisance parameters. The resulting values represent the χ^2 function values at i^{th} bin of channel c (e.g. the fourth energy bin on the channel $\nu_\mu \to \nu_e$). The total χ^2 function of an experiment is determined by summing up the χ^2 values of different channels and minimizing the result over a set of oscillation parameters given by the user. Depending on the objectives of simulation task, the number of minimized oscillation parameters defines the accuracy of the simulation, the greater number providing generally more realistic results with the cost of longer simulation time.

The χ^2 minimizers typically return distributions that are smooth manifolds, as it is the case for superbeams, but this is not always so. The minimizing algorithms find minimum points locally, which means that experiments of more complicated topology, such as the neutrino factory for example, need often more detailed information to avoid the possibility of missing some local minimums. This process can be helped by limiting the study to the specific part of the manifold of best fit parameter values one wants to study. To do this, GLoBES allows to set constraints to the oscillation parameters through so called priors. In this work we compute the priors with the following formula:

$$\begin{aligned}\chi^2_{\text{prior}} = &\left(\frac{|\Delta m^2_{31}(\omega)| - |\Delta m^2_{31}(\omega_0)|}{\sigma(|\Delta m^2_{31}|)}\right)^2 + \left(\frac{\theta_{13}(\omega) - \theta_{13}(\omega_0)}{\sigma(\theta_{13})}\right)^2 \\ &+ \left(\frac{\Delta m^2_{21}(\omega) - \Delta m^2_{21}(\omega_0)}{\sigma(\Delta m^2_{21})}\right)^2 + \left(\frac{\theta_{12}(\omega) - \theta_{12}(\omega_0)}{\sigma(\theta_{12})}\right)^2 \\ &+ \left(\frac{\theta_{23}(\omega) - \theta_{23}(\omega_0)}{\sigma(\theta_{23})}\right)^2 + \left(\frac{\hat{\rho} - 1}{\sigma(\hat{\rho})}\right)^2 .\end{aligned} \tag{15}$$

The prior function (15) adds the appropriate corrections to the χ^2 in Eq. (14) using the test and true values ω and ω_0 and 1 σ errors, respectively. As for the matter density parameters, $\hat{\rho}$ represents the density value over average ratio $\hat{\rho} = \rho/\rho_0$ and $\sigma(\hat{\rho})$ relates to its uncertainty. The true values and their errors usually taken as input from the best fit values similar to the ones presented in Sec. 1.1.

GLoBES considers the event rates in neutrino experiments in so called rules, which contain the event rate information from signal and background and accounts corresponding systematic errors. The overall χ^2 function is calculated by summing the minimized pull functions for all channels in each rule and

combine different rules to obtain χ^2 value for a complete neutrino experiment. The χ^2 values of a set of different experiments can also be added together, giving a total χ^2 estimate for that set of experiments. The corrections coming from priors are set by adding the prior function values χ^2_{prior} to the result. The total χ^2 function is therefore obtained using Eq. (14) and (15):

$$\chi^2_{\text{total}} = \sum_{\text{experiments}} \sum_{\text{rules}} \sum_{\text{channels}} \min_{\omega} \left[\chi^2_{\text{pull}}(\omega, \omega_0, \zeta_1, \ldots, \zeta_k) + \chi^2_{\text{prior}}(\omega, \omega_0) \right]. \tag{16}$$

When calculating χ^2 for a set of experiments, one has to note that the systematics are added only once in the calculation process, meaning that the resulting χ^2 distributions might not be equal to a sum of χ^2 values computed from each experiment separately. The system also assumes the systematics to be independent among different rules. Therefore one has to be careful when comparing different χ^2 distributions.

The computation of χ^2 is a straightforward process, which can be carried out with a modern computer in reasonable time. The newer versions of GLoBES, namely 3.0 and above, allow user-definitions of priors and systematics. To perform the computing in a reasonable time, the system employs a local minimizer to perform the pull method in Eq (14). This often necessitates external information to guide the minimizer.

5 Defining experiments on abstract level

Simulation routines are designed to be run on abstractions of neutrino experiments, which are provided in special glb-files in Advanced Experiment Definition Language. Using the benefits of this experiment definition language, we create sample AEDL files to describe the behaviour of LENA and GLACIER detectors in the 2288-km-long CERN-Pyhäsalmi baseline. The discussion goes systematically through the definition of the neutrino flux, simulation of matter densities, cross sections, energy resolution and finally the channel and rule description.

5.1 Neutrino fluxes and cross sections

GLoBES runs on a modular structure which applies pieces of information that are often produced with different simulators. Many variables also accept input

in more than one way, which was the case with input of the source power in Eq. (8) for example. The process thus requires proper normalization in experiment definition. The normalization factor is calculated by relating different units in the generic event rate computation formula Eq. (9) so that the units match together in different files.

In the numerical work of this study, we choose to use neutrino fluxes provided by A. Longhin [48, 49], which represent the simulated fluxes of a HP-PS2 neutrino beam on a 2300-km-long baseline. The neutrino fluxes are given in distinctive dat-files, which contain neutrino fluxes as a function of neutrino energy. We also use the charged current and neutral current cross section files that are included in the standard GLoBES package [50, 51]. These files present cross sections for charged and neutral current events per nucleon, and assume a 10^{-37} cm^2 unit. The neutrino fluxes, on the other hand, are presented for a reference surface area A at a reference distance L. The other parameters GLoBES uses to calculate event rates are the bin width ΔE and integrated luminosity $\mathcal{L}$. Also the number of target particles τ per detector unit mass m_u is needed.

In GLoBES versions 3.0 and higher the undocumented fudge factor in Eq. (9) is removed, so the normalization factor is defined as

$$\texttt{@norm} = \left(\frac{\text{GeV}}{\Delta E}\right)\left(\frac{\text{cm}^2}{A}\right)\left(\frac{L}{\text{km}}\right)^2\left(\frac{\tau}{m_u}\right) \times 10^{-38} \times \left(\frac{\mathcal{L}_u}{\mathcal{L}}\right), \qquad (17)$$

where ΔE, A, L, τ and $\mathcal{L}$ are to be converted to units GeV, cm^2, km, m_u and $\mathcal{L}_u$, respectively. Since we are simulating superbeams, for which the detector masses are given in kilotons and the number of useful protons on target per year (POT yr^{-1}), we can choose $m_u = 1\,\text{kton}$ and $\mathcal{L}_u = 1\,\text{POT}\,\text{yr}^{-1}$.

The fluxes are optimized to peak at approximate 4.5 GeV energy for 2300 km baseline, using a 10×10 m^2 reference surface area at 100 km distance from the source. The fluxes are provided for 3.0×10^{21} protons on target per operational year, which is in accordance with Sec. 3.1. The energies are simulated for 0 to 10 GeV, divided in 20 equidistant energy bins. The cross section files provide the cross section values per useful nucleons, which is $6.022 \times 10^{23} \cdot 10^9$ nucleons per kiloton for a fully active detector liquid.

Let us first calculate the normalization factor for LENA. The liquid scintillator detector is not fully active, but contains 43.5 kilotons of active scintillator in a total of 50 kilotons of liquid (cf. [22]). The normalization factor for LENA is therefore

$$\texttt{@norm} = \left(\frac{\text{GeV}}{\Delta E}\right)\left(\frac{\text{cm}^2}{A}\right)\left(\frac{L}{\text{km}}\right)^2\left(\frac{\tau}{m_u}\right) \times 10^{-38} \times \left(\frac{\mathcal{L}_u}{\mathcal{L}}\right)$$

$$= \left(\frac{\text{GeV}}{0.5\,\text{GeV}}\right) \cdot \left(\frac{\text{cm}^2}{10^6\,\text{cm}^2}\right) \cdot \left(\frac{100\,\text{km}}{\text{km}}\right)^2 \cdot \left(\frac{43.8}{50.0} \cdot 6.022 \cdot 10^{23} \cdot 10^9\right)$$

$$\cdot 10^{-38} \cdot \left(\frac{1\,\text{POT}\,\text{yr}^{-1}}{3.0 \cdot 10^{21}\,\text{POT}\,\text{yr}^{-1}}\right) = 3.516848 \cdot 10^{-29}.$$

The normalization factor for GLACIER is calculated in similar fashion, the only difference being that the liquid argon substance is fully active:

$$\texttt{@norm} = \left(\frac{\text{GeV}}{0.5\,\text{GeV}}\right) \cdot \left(\frac{\text{cm}^2}{10^6\,\text{cm}^2}\right) \cdot \left(\frac{100\,\text{km}}{\text{km}}\right)^2 \cdot \left(6.022 \cdot 10^{23} \cdot 10^9\right)$$

$$\cdot 10^{-38} \cdot \left(\frac{1\,\text{POT}\,\text{yr}^{-1}}{3.0 \cdot 10^{21}\,\text{POT}\,\text{yr}^{-1}}\right) = 4.014667 \cdot 10^{-29}.$$

With these normalization factors it is possible to define neutrino experiments by simply stating the general parameters that make the neutrino experiment unique. For instance, we may define an experiment with 2288-km-long baseline and 50 kton neutrino detector by issuing `@target_mass = 50.0`, `@baseline = 2288` in corresponding glb-file. The description files use the same units that have been assumed in the normalization factor calculation, i.e. we have to define energies in gigaelectronvolts, baselines in kilometres and running times in years. Beam powers are similarly given in useful proton decays per year.

Table 1: Basic AEDL parameters

Detector	LENA	GLACIER
Target mass (kt)	50	100
Baseline (km)	2290	
Running time (yr)	5 + 5	
Parent decays (POT yr^{-1})	3.0×10^{21}	
Normalization (10^{-29})	3.516826	4.014667

As per Sec. 3.1, the CN2PY beam is planned to have 3.0×10^{21} yearly production of 50 GeV protons with approximately 2290-km-long baseline and 5+5 years of neutrino and antineutrino running, which would yield approximately matching numbers of neutrino and antineutrino events. Previous simulation studies, e.g. [42] and [46], have shown that 5+5 years is also sufficient to provide adequate results with the proposed neutrino experiments. In fact, the antisymmetric running times do not seem to yield any significant advantage. Therefore we decide to use 5 years of neutrino run and 5 years for antineutrino run in the simulations we perform in this paper. The general experiment parameters in our simulation study are summarized in Tab. 1.

5.2 Density maps

The matter density profile can be presented in a few different methods in GLoBES. The most common choices are to either insert an average matter density or place a manually defined density map to estimate electron density parameter N_e that is present in the transition probability formula shown in Eq. (4). Another method is to define the density map with the so called preliminary reference earth model PREM [52] which simulates the matter density by approximating the Earth to a series of layers. The PREM method is fairly accurate; the matter density map illustrating the CERN-to-Pyhäsalmi baseline is presented in Fig. 3. In the same graph a sample PREM-computed density map is also given, approximating the distribution in 32 steps.

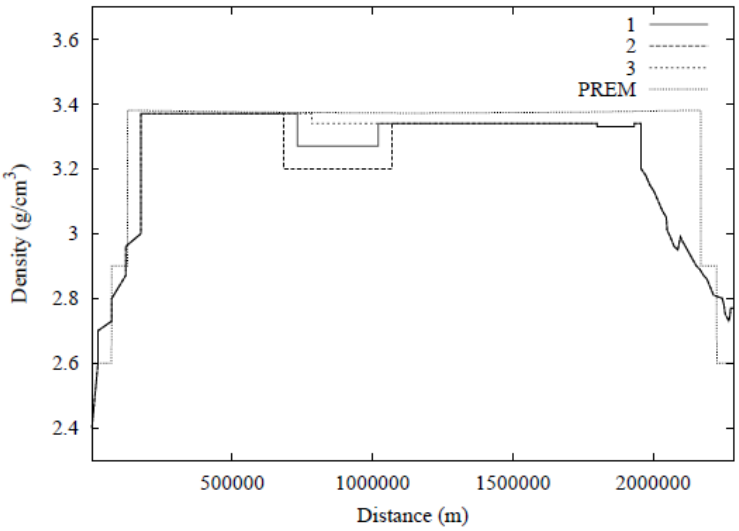

Figure 3: Real density versus PREM-computed densities mapped along the CERN-to-Pyhäsalmi baseline [53].

The realistic density model has some uncertainty within the distances 730 km - 1010 km where the ground turns to astenosphere and the average matter density can vary between 3.27, 3.20 and 3.34 $\mathrm{g\,cm^{-3}}$. These alternatives are shown as curves (1), (2) and (3), respectively, in Fig. 3. As such, simulations with the realistic density map can be assigned with a 1% error estimate [53].

The PREM computation provides comparable accuracies, and a 2% error estimate should suffice [54]. In this study we choose to use PREM model with 20 approximation steps to save computation time, and establish a 2% error to this parameter in simulations.

5.3 Energy resolution and binning

The process of registering a neutrino event in a detector is a rather complex topic as a neutrino event is never observed directly. Detector instrumentation uses the information obtained from observing the emerging secondary particles to reconstruct the neutrino event and determine the initial energy and flavour of the incident neutrino. The reconstructed energy is normally distributed with some standard deviation and mean value, and the shape of this distribution is determined by the properties of the detector. At the numerical level this ability is parametrized with the so called energy resolution function, which is integrated over the event rate computation phase.

The event rate formula shown in Eq. (5) takes into account the effect of the Gaussian error induced by the reconstruction process with the so called bin kernel function which integrates the Gaussian function over bin width ΔE_i in channel c:

$$K(E, E') = \int_{E_i - \Delta E_i/2}^{E_i + \Delta E_i/2} dE' \; \frac{1}{\sigma(E)\sqrt{2\pi}} e^{\frac{(E-E')^2}{2\sigma^2(E)}}. \tag{18}$$

The bin kernel formula (18) shows the connection between the true and reconstructed energies E and E' of the interacting neutrino. The standard deviation of the reconstructed energy is given by $\sigma(E)$, which is defined in the AEDL syntax as follows:

$$\sigma(E) = \alpha \cdot E + \beta \cdot \sqrt{E} + \gamma, \tag{19}$$

where α, β and γ are positive constants. In a superbeam experiment, for instance, neutrino energy E is given in GeV and α, β and γ are defined such that $\sigma(E)$ is given in GeV (e.g. a $0.05\,E$ energy resolution is given by $\alpha = 0.05$,

$\beta = 0$, $\gamma = 0$). The smaller α, β, γ values indicate the smaller deviation in reconstructed energies and yield the better accuracies.

Table 2 lists the AEDL parameters that we generally use to define detection properties in our simulations, unless stated otherwise. The exact form of the standard deviation function in Eq. (19) is generally not known, but a recent simulation study on LENA suggests a general dependence of $\sigma(E) = 0.05\,E$ for both muon and electron neutrino interactions at all but the lowest energies [22, 23]. The detection efficiencies for these neutrino events are set to 50%, which is an educated guess based on similar simulation studies (see [42] for an example). Similarly GLACIER is expected to be $\sigma(E) = 0.20\,E$ in both the muon neutrino and antineutrino channels and 0.15 in the electron neutrino and antineutrino channels. The efficiency in GLACIER is set to 90% for both muon and electron neutrino states [42]. See Ch. 3.2 and Ch. 3.3 for more details.

Energy resolution functions are not the only distinguishing elements that are different in LENA and GLACIER, but the energy scopes are different as well. We set LENA to scan energies within [0.5, 7.0] GeV energy range and GLACIER to [0.1, 10.0] GeV, respectively. The energy scope is divided into 80 bins of 0.125 GeV width from [0, 10] GeV energy range, giving us $\Delta E_i = 0.125\,\text{GeV}$ for $i = 1, 2, \ldots, 80$. At the studied energies we may keep the energy resolution of LENA at $\sigma(E) = 0.05\,E$ throughout the simulation. As a LArTPC detector, GLACIER has a much smaller energy threshold. Hence we may keep its energy resolution functions at $0.20\,E$ (muon) and 0.15 (electron) at all energies. LENA has therefore slightly better resolution at small energies, whilst GLACIER outperforms LENA at $\nu_e/\bar{\nu}_e$ detection at very high energies.

When determining the energy resolution function, one has to notice that the automatic bin based method and the sigma function formalism are a rather crude approximate model that does not take into account the sophisticated energy dependencies that become particularly important at low energies, $E \lesssim 100\,\text{MeV}$. The more secure way to perform calculations require the use of the

Table 2: Detector parameters

Detector	LENA	GLACIER
$\nu_\mu/\bar{\nu}_\mu$ efficiency (%)	50	90
$\nu_e/\bar{\nu}_e$ efficiency (%)	50	90
Energy resolution for ν_e (GeV)	$0.05\,E$	0.15
Energy resolution for ν_μ (GeV)	$0.05\,E$	$0.20\,E$
Energy window (GeV)	[0.5, 7.0]	[0.1, 10.0]
Number of bins	80	80

so called migration matrices, which are generally simulated with other Monte Carlo simulator packages. For the LENA simulations one could use e.g. [55]. Nevertheless, in the simulation of superbeams we consider the built-in automatic model sufficient due to the fairly simple experiment topology.

5.4 Channels and rules

The standard three-flavour superbeam experiments are focused on observing neutrino events through channels $\nu_\mu \rightarrow \nu_e$ and $\nu_\mu \rightarrow \nu_\mu$ and the corresponding antiparticle channels. The efficiencies of different detector setups are tested with simulation studies computing event rates for each channel in every energy bin. To achieve this, the simulator has to estimate the event rates for all possible oscillations and take into account all possible interactions. At the experiment description level, the scrutinized signal and background rates are given in rules using the rates of the distinct neutrino channels, which are finally multiplied by the detector efficiency to obtain the total rates (see below for an example).

In this paper we study the performance of LENA and GLACIER detectors in determining the electron appearance and muon disappearance rates that involve the charged current (CC) interaction where ν_e and e^- exchange a $W^\pm$ boson. The composition of observed signal and background rates is given in AEDL rules summarized in Tab. 3 and Tab. 4. The muon neutrino beam is accompanied with small $\bar{\nu}_\mu$, ν_e and $\bar{\nu}_e$ components as side products of the pion decay process. Similarly the $\bar{\nu}_\mu$ beam is contaminated with ν_μ, ν_e and $\bar{\nu}_e$, which may all oscillate and interact via both CC and NC reactions in the detector. These additional particles disturb the process of observing signal particles, and they are therefore taken as background. Further uncertainty to the signal event count comes from the limitations of the detectors, including the risk of misidentifying NC events as their CC counterparts, which concerns the muon disappearance channels in particular.

Let us first give a simple description of the signal and background event rate composition in LENA. Following the experiment details given in Sec. 3.2, we set the simulator to compute signal events in LENA in the ν_e appearance and ν_μ disappearance channels $(\nu_\mu \rightarrow \nu_e)_{\mathrm{CC}}$ and $(\nu_\mu \rightarrow \nu_\mu)_{\mathrm{CC}}$ at 50% efficiency. The only exception to the 50% sensitivity comes from the NC muon neutrino events which are accidentally detected and misidentified as CC events at 5% chance. The low acceptance rate is possible due to the information that comes from the arrival times of incoming neutrinos [55], a feature that is available for both liquid scintillator and LArTPC detectors. In similar manner we set the muon antineutrino beam yield signal events in antineutrino channels $(\bar{\nu}_\mu \rightarrow \bar{\nu}_e)_{\mathrm{CC}}$

and $(\bar{\nu}_\mu \rightarrow \bar{\nu}_\mu)_{\mathrm{CC}}$. The background is determined by all possible CC and NC events at which the final state is of the same flavour as the signal particle i.e. electron appearance rules get backgrounds from ν_e and $\bar{\nu}_e$ particles and muon disappearance rules from ν_μ and $\bar{\nu}_\mu$ particles.

The composition of GLACIER rates are presented similarly. The appearance and disappearance rules are identical to LENA except for the detection efficiencies, which are significantly better in GLACIER. Following detector specifications given in Sec. 3.2, we simulate GLACIER detecting neutrinos and antineutrinos at 90% rate. The NC event rejection is set to remarkable 99.5% efficiency, meaning that only 0.5% of all muon neutrinos and antineutrinos interacting through NC reaction are erroneously accepted [42, 46]. In this case the detector does not see difference between particles and antiparticles, unless the detector is magnetized.

As discussed in Sec. 4.2, neutrino detectors are also subject to various systematic errors. In this study we describe the energy normalization error with a simple pull to both signal and background rates using weights π^a and π^b, respectively (see Eq. (15)). We also define an energy calibration error to both the sig-

Table 3: Neutrino and antineutrino rules in LENA.

ν_e appearance rule	
Signal	$0.5 \times (\nu_\mu \rightarrow \nu_e)_{\mathrm{CC}}$
Background	$0.5 \times (\nu_e \rightarrow \nu_e)_{\mathrm{CC}} + 0.5 \times (\bar{\nu}_e \rightarrow \bar{\nu}_e)_{\mathrm{CC}}$ $+ 0.5 \times (\bar{\nu}_\mu \rightarrow \bar{\nu}_e)_{\mathrm{CC}} + 0.5 \times (\nu_e \rightarrow \nu_e)_{\mathrm{NC}}$ $+ 0.5 \times (\bar{\nu}_e \rightarrow \bar{\nu}_e)_{\mathrm{NC}}$
ν_μ disappearance rule	
Signal	$0.5 \times (\nu_\mu \rightarrow \nu_\mu)_{\mathrm{CC}}$
Background	$0.5 \times (\bar{\nu}_\mu \rightarrow \bar{\nu}_\mu)_{\mathrm{CC}} + 0.05 \times (\nu_\mu \rightarrow \nu_\mu)_{\mathrm{NC}}$ $+ 0.05 \times (\bar{\nu}_\mu \rightarrow \bar{\nu}_\mu)_{\mathrm{NC}}$
$\bar{\nu}_e$ appearance rule	
Signal	$0.5 \times (\bar{\nu}_\mu \rightarrow \bar{\nu}_e)_{\mathrm{CC}}$
Background	$0.5 \times (\nu_e \rightarrow \nu_e)_{\mathrm{CC}} + 0.5 \times (\bar{\nu}_e \rightarrow \bar{\nu}_e)_{\mathrm{CC}}$ $+ 0.5 \times (\nu_\mu \rightarrow \nu_e)_{\mathrm{CC}} + 0.5 \times (\nu_e \rightarrow \nu_e)_{\mathrm{NC}}$ $+ 0.5 \times (\bar{\nu}_e \rightarrow \bar{\nu}_e)_{\mathrm{NC}}$
$\bar{\nu}_\mu$ disappearance rule	
Signal	$0.5 \times (\bar{\nu}_\mu \rightarrow \bar{\nu}_\mu)_{\mathrm{CC}}$
Background	$0.5 \times (\nu_\mu \rightarrow \nu_\mu)_{\mathrm{CC}} + 0.05 \times (\nu_\mu \rightarrow \nu_\mu)_{\mathrm{NC}}$ $+ 0.05 \times (\bar{\nu}_\mu \rightarrow \bar{\nu}_\mu)_{\mathrm{NC}}$

Table 4: Neutrino and antineutrino rules in GLACIER.

ν_e appearance rule	
Signal	$0.9 \times (\nu_\mu \to \nu_e)_{\mathrm{CC}}$
Background	$0.9 \times (\nu_e \to \nu_e)_{\mathrm{CC}} + 0.9 \times (\bar{\nu}_e \to \bar{\nu}_e)_{\mathrm{CC}}$ $+ 0.9 \times (\bar{\nu}_\mu \to \bar{\nu}_e)_{\mathrm{CC}} + 0.9 \times (\nu_e \to \nu_e)_{\mathrm{NC}}$ $+ 0.9 \times (\bar{\nu}_e \to \bar{\nu}_e)_{\mathrm{NC}}$
ν_μ disappearance rule	
Signal	$0.9 \times (\nu_\mu \to \nu_\mu)_{\mathrm{CC}}$
Background	$0.9 \times (\bar{\nu}_\mu \to \bar{\nu}_\mu)_{\mathrm{CC}} + 0.005 \times (\nu_\mu \to \nu_\mu)_{\mathrm{NC}}$ $+ 0.005 \times (\bar{\nu}_\mu \to \bar{\nu}_\mu)_{\mathrm{NC}}$
$\bar{\nu}_e$ appearance rule	
Signal	$0.9 \times (\bar{\nu}_\mu \to \bar{\nu}_e)_{\mathrm{CC}}$
Background	$0.9 \times (\nu_e \to \nu_e)_{\mathrm{CC}} + 0.9 \times (\bar{\nu}_e \to \bar{\nu}_e)_{\mathrm{CC}}$ $+ 0.9 \times (\nu_\mu \to \nu_e)_{\mathrm{CC}} + 0.9 \times (\nu_e \to \nu_e)_{\mathrm{NC}}$ $+ 0.9 \times (\bar{\nu}_e \to \bar{\nu}_e)_{\mathrm{NC}}$
$\bar{\nu}_\mu$ disappearance rule	
Signal	$0.9 \times (\bar{\nu}_\mu \to \bar{\nu}_\mu)_{\mathrm{CC}}$
Background	$0.9 \times (\nu_\mu \to \nu_\mu)_{\mathrm{CC}} + 0.005 \times (\nu_\mu \to \nu_\mu)_{\mathrm{NC}}$ $+ 0.005 \times (\bar{\nu}_\mu \to \bar{\nu}_\mu)_{\mathrm{NC}}$

nal and background rates using weights π^c and π^d. A mildly optimistic guess for this systematic error is 5% for normalization errors and 2.5% for calibration errors [42, 46], which we apply by setting $\pi^a, \pi^b = 0.05$ and $\pi^c, \pi^d = 0.025$ in the test rate formula in Eq. (13). More conservative choices may vary from 10% through 15% [54, 56] for the normalization error, but we consider 5% sufficient for the first simulations of the CN2PY setup, which handles mainly high energetic beams.

6 Data analysis

In this section we present a collection of simulations that are performed to probe the potential of a long baseline neutrino experiment in the CERN-to-Pyhäsalmi beamline as it would appear in the light of the present knowledge on the oscillation parameters. The numerical study is carried out with GLoBES functions, which provide an approximate but quick analysis tool to evaluate the performance of different experiment setups. In this section we test LENA and GLACIER detectors combined with the HP-PS2 beam on the CERN-to-Pyhäsalmi baseline. The study begins with analysing neutrino fluxes, transi-

tion probabilities and event rates and continues with testing measurable $\sin^2 2\theta_{13}$ and δ_{CP} ranges with $\Delta\chi^2$ statistics. The analysis also unveils mass hierarchy and CP violation discovery potentials under different $\sin^2 2\theta_{13}$ and δ_{CP} values and studies sensitivities to solve the $(\theta_{23}, 90° - \theta_{23})$ degeneracy.

6.1 Event rates

In our study we use the CN2PY neutrino fluxes simulated for the 2300 km CERN-to-Pyhäsalmi baseline [48, 49]. The flux files were introduced in Sec. 4.1 and the spectrum of the neutrino beam flux is presented in Fig. 4. The left panel shows the beam composition of the neutrino beam and the right panel illustrates the muon neutrino component at different baselines. The neutrino fluxes are provided in two files, which give the ν_μ and $\bar{\nu}_\mu$ beam contents separately.

The ν_μ beam contains approximately 4% of $\bar{\nu}_\mu$, 1% of ν_e and 0.1% of $\bar{\nu}_e$, and the ν_μ flux variation depends on the baseline, as shown in the figure. Similarly the $\bar{\nu}_\mu$ beam is contaminated with 4% of ν_μ, 1% of $\bar{\nu}_e$ and 0.1% of ν_e. In the antineutrino beam content is thus presented by a similar plot as given for the neutrino beam in Fig. 4, only the flavour ordering is different. This contamination is known as the so called intrinsic background, and it is considered irreducible.

Let us first compute the probabilities for one flavour state to oscillate to another on the way from source to detector. The CN2PY beam is designed to study the muon neutrino transition to electron neutrino and vice versa. Therefore the flux files have been optimized assuming no sensitivity for tau neutri-

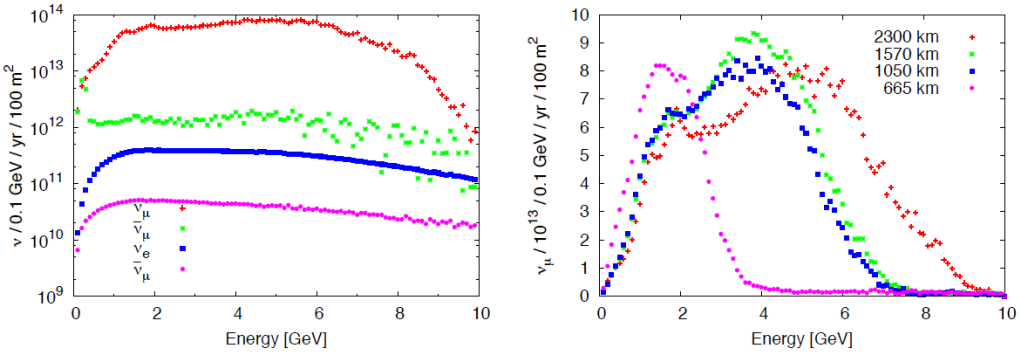

(a) ν beam spectrum for 2300 km.

(b) ν_μ content of different beams.

Figure 4: Composition of the neutrino beam in HP-PS2 as shown in the flux files [48]. The left panel shows the composition of the neutrino beam optimized for the 2300-km-long CN2PY baseline. The right panel presents the same spectrum for candidate baselines varying from 665 km to 2300 km.

nos at all, and we conformingly ignore all tau neutrino oscillations in this study. The transition probabilities are calculated with the simulator using a probability formula that is equivalent to the one that was presented in Eq. 4 in Sec. 1.2. Since the signal events will be determined by the leading term $\sin^2 2\theta_{13} \sin^2 \theta_{23} \sin^2((1-\hat{A})\Delta)/(1-\hat{A})^2$, we are focusing on studying the components $\sin^2 2\theta_{13}$ and $\sin^2 \theta_{23}$ in particular.

For the oscillation parameters we make a guess for what the real oscillation parameter values are and name them the true values. This set is presented in Tab. 5. The true values are taken from the best-fit values obtained from the measurements with the previous neutrino experiments, which were shown at the beginning of Ch. 1. We also assume $\sin^2 2\theta_{13} \cong 0.1$ for the first mixing angle and let the CP violation phase δ_{CP} vary through its possible values $-180°, \ldots, 180°$. These parameter choices are in agreement with the results extracted from previous experiment data. The errors represent the quantities for the corresponding Gaussian functions. Here one has to note that the errors are set for $\sin^2 \theta_{12}$, $\sin^2 2\theta_{13}$ and $\sin^2 \theta_{23}$ instead of θ_{12}, θ_{13} and θ_{23}.

In the following simulations we compute transition probabilities assuming the aforementioned parameter values. For illustration we computed the probabilities here with standard GLoBES values (cf. [12, 13]) for oscillation parameters and present the results in Fig. 5 and Fig. 6.

When the oscillation parameters are allowed to vary in probability plots as described above, the transition probabilities deviate as function of δ_{CP} and $\mathtt{sgn}[\Delta m^2_{31}]$. The determination of the mass hierarchy is based on the fact that normal hierarchy and inverted hierarchy lead to different oscillation probabilities. When energy is high enough, the probabilities for NH and IH cease to overlap, allowing to distinguish between hierarchies. This is maximized at the magic energies.

Table 5: Simulated oscillation parameters

Parameter	Central value	Error value
$\sin^2 \theta_{12}$	0.312	5%
$\sin^2 2\theta_{13}$	0.1	5%
$\sin^2 \theta_{23}$	0.51	10%
Δm^2_{21}	$7.6 \times 10^{-5}\,\mathrm{eV}^2$	3%
Δm^2_{31} (NH)	$2.45 \times 10^{-3}\,\mathrm{eV}^2$	5%
Δm^2_{31} (IH)	$-2.34 \times 10^{-3}\,\mathrm{eV}^2$	5%
$\hat{\rho}$	1.0	2%

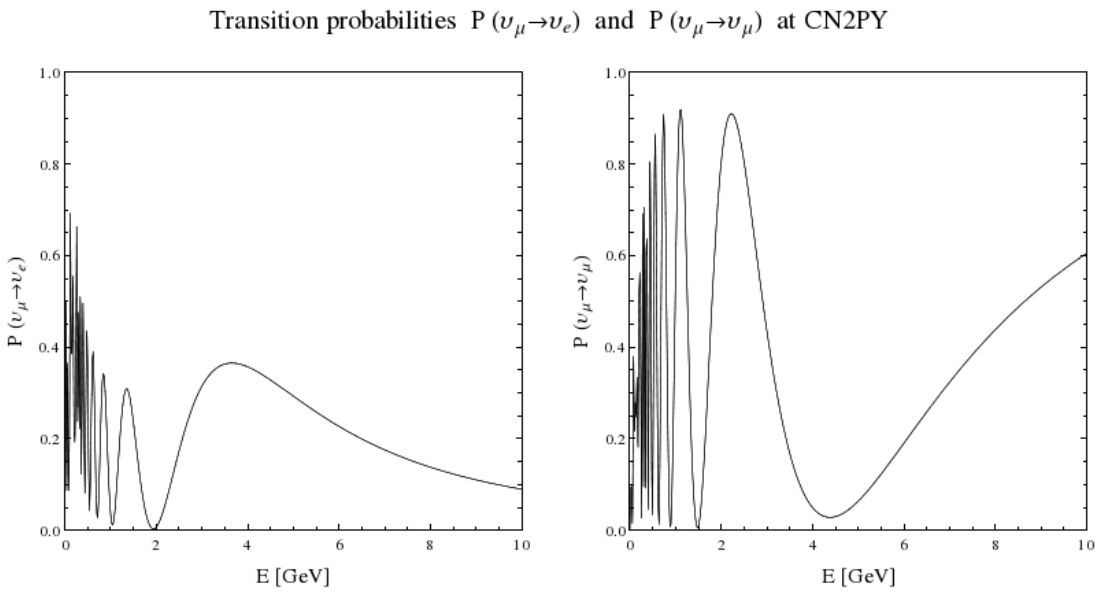

Figure 5: The probabilities of $\nu_\mu \to \nu_e$ and $\nu_\mu \to \nu_\mu$ transitions in the CN2PY baseline, as simulated with GLoBES using the LENA setup.

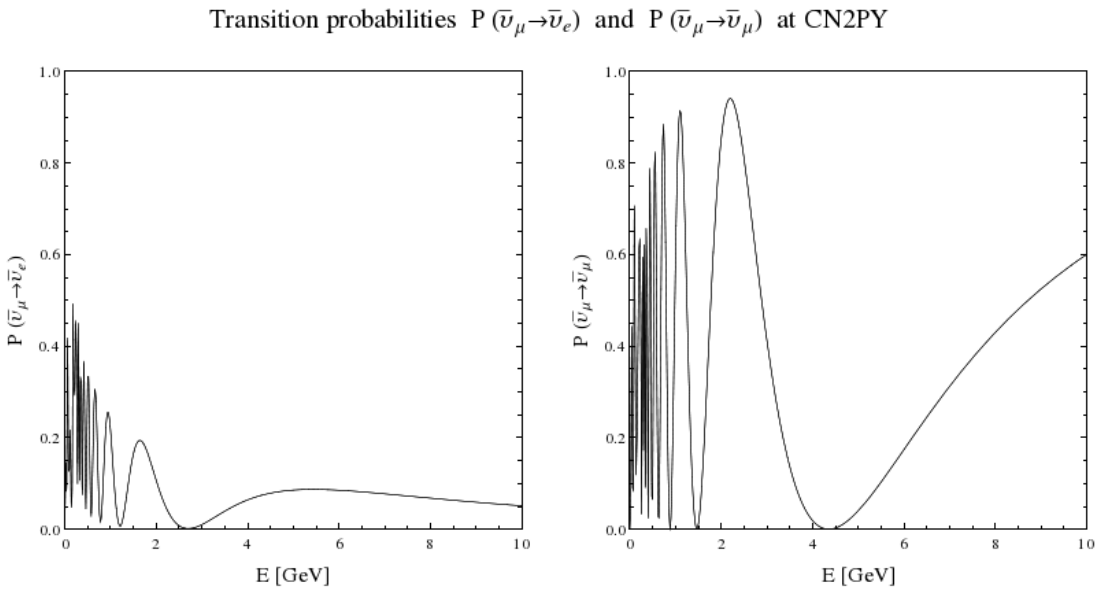

Figure 6: The probabilities of $\bar{\nu}_\mu \to \bar{\nu}_e$ and $\bar{\nu}_\mu \to \bar{\nu}_\mu$ transitions in the CN2PY baseline, as simulated with GLoBES using the LENA setup.

Neutrino fluxes and oscillation probabilities are vital elements when one calculates the rates of the possible neutrino events that occur in the neutrino detector. Applying the methods described in Sec. 4.1, we use the experiment definitions of LENA and GLACIER to simulate the event rates that could be expected from the planned experiment on the basis of the three-flavour neutrino theory. GLoBES has a special function for obtaining this piece of low level information. We ran the software to provide event rates for each rule that was introduced in Sec. 5.4. The results are shown in Fig. 7 for LENA and Fig. 8 for GLACIER.

The event rates are plotted in four frames in each experiment, one for every pair of signal and background. The event rates were initially simulated as events per energy bin, and the intermediate values were calculated using interpolation. In the ν_e appearance rules the signal rates show as continuous spectrum with two maximums. The flux files we are using for neutrinos are optimized for the first maximum, which appears at approximately 4.7 GeV energy in simulations that were done for both LENA and GLACIER. The neutrino beam is optimized to peak at this magic energy in order to maximize neutrino statistics in appearance rules. The statistical analysis is slightly disturbed by the background, which consist of misidentified NC events and the intrinsic beam background. Fig. 7 and Fig. 8 show that the number of background events is relatively small in comparison with the signal events at most energies in the GeV scale.

Besides the ν_e appearance rule, the event rate statistics is also obtained from the ν_μ disappearance signals. The other available channels are the respective antineutrino rules which give complementary information to the data. The plots are for antineutrinos similar to those of the neutrinos, except the event numbers are smaller and the peak energies move to 5.7 GeV.

The second oscillation maxima are at the energies 1.35 GeV and 1.75 GeV for the ν_e and $\bar{\nu}_e$ appearance, respectively. Although the neutrino experiments are optimized for the first oscillation maximum, the second maxima are useful for extracting complementary information [54].

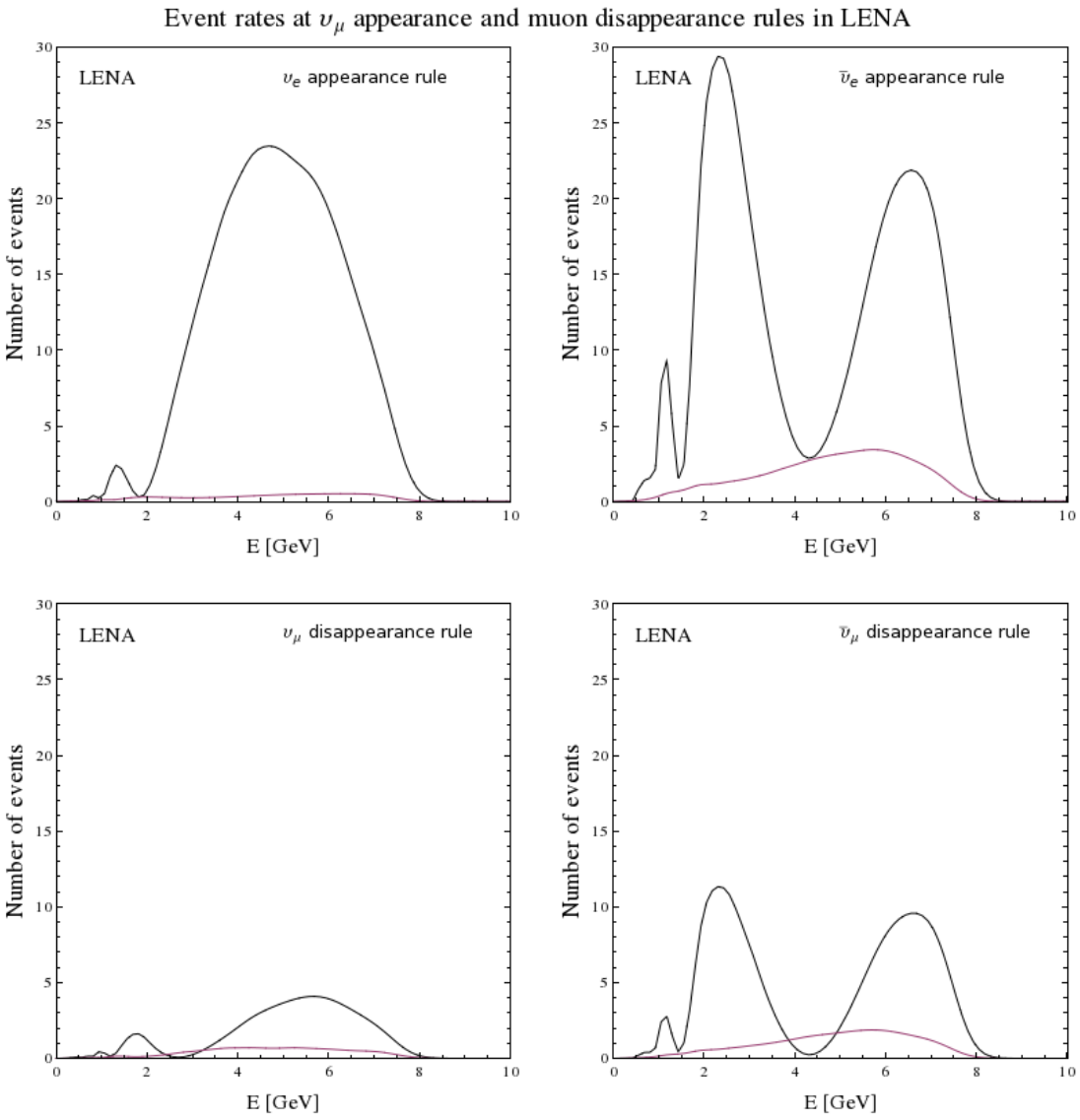

Figure 7: Event rates for neutrino signals and backgrounds in LENA. The panels show the rates for ν_e and $\bar{\nu}_e$ appearance and ν_μ and $\bar{\nu}_\mu$ disappearance. Signal rates are plotted in black and the backgrounds in colors.

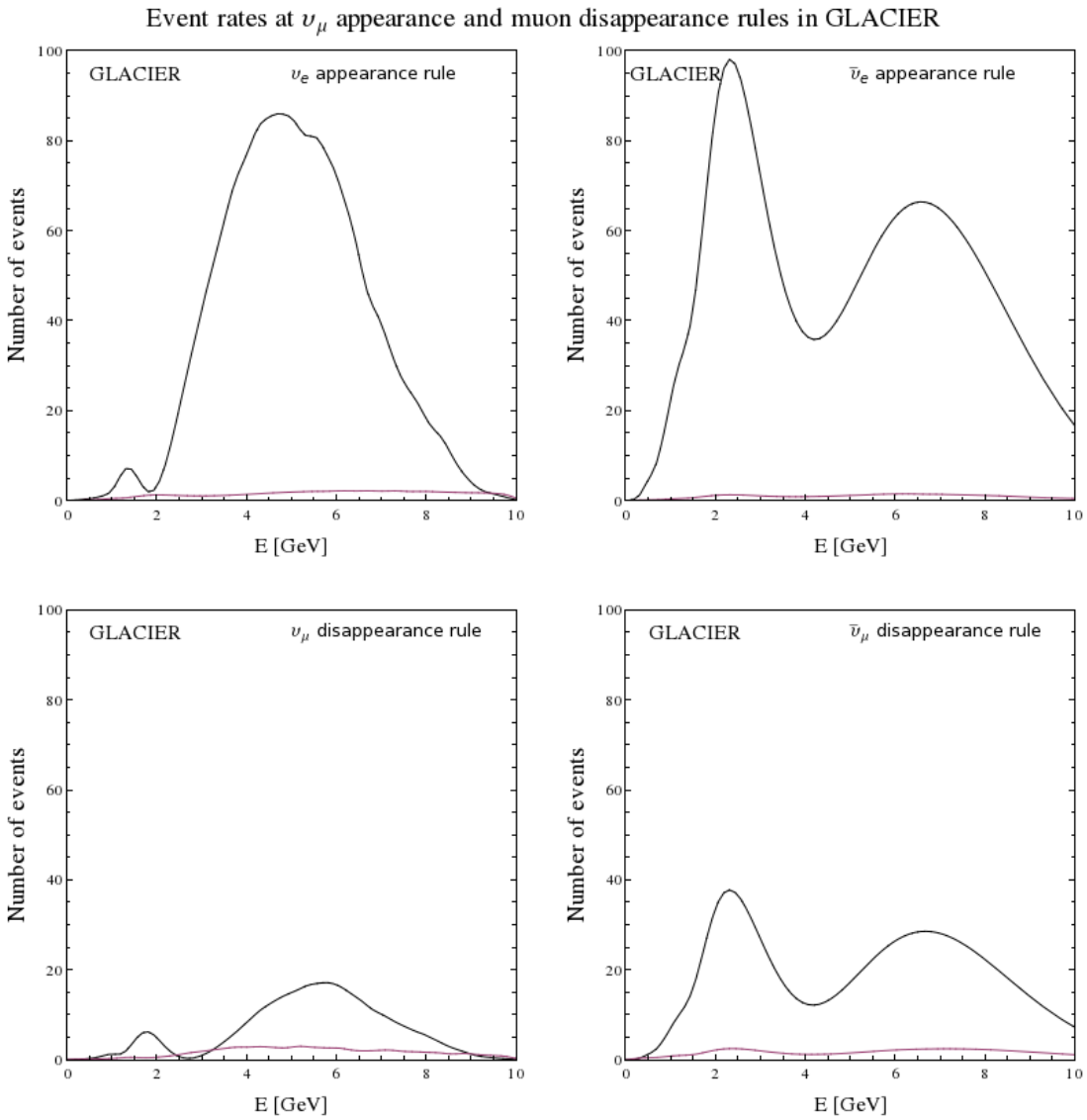

Figure 8: Event rates for neutrino rules at GLACIER. The panels show the signal and background rates for ν_e and $\bar{\nu}_e$ appearance and also ν_μ and $\bar{\nu}_\mu$ disappearance. The signal events are in black and the background in colour.

6.2 Allowed parameter ranges

Parameter degeneracies rise from the inability to disentangle different oscillation parameters from each other so that they could be determined individually from the experimental data. It can occur that several different value sets of parameters lead to the same values for an observable quantity. More uncertainty arises when the parameter values are assigned with error limits, causing parameter correlations that need to be taken into account. In this section we are interested in seeing how this disinformation affects the sensitivity to $\sin^2 2\theta_{13}$ and δ_{CP} measurements in the simulated neutrino experiments and compute the χ^2 statistics using Eq. (16) to illustrate the correlation between the two parameters.

Let us now create the graphs that show the allowed values of $\sin^2 2\theta_{13}$ and δ_{CP} that can be measured in the studied experiments. The data is simulated by testing different ($\sin^2 2\theta_{13}$, δ_{CP}) combinations and comparing the resulting event rates to those computed from alleged true parameter values. The graphs were produced by varying the test values of $\sin^2 2\theta_{13}$ and δ_{CP} and comparing the resulting event rates with those computed from the true values. In Fig. 9 these values are plotted using the same true values we used in the case of computing transition probabilities and event rates in Sec. 6.1 and assuming the maximum CP violation by setting $\delta_{\mathrm{CP}} = 90°$ and $-90°$.

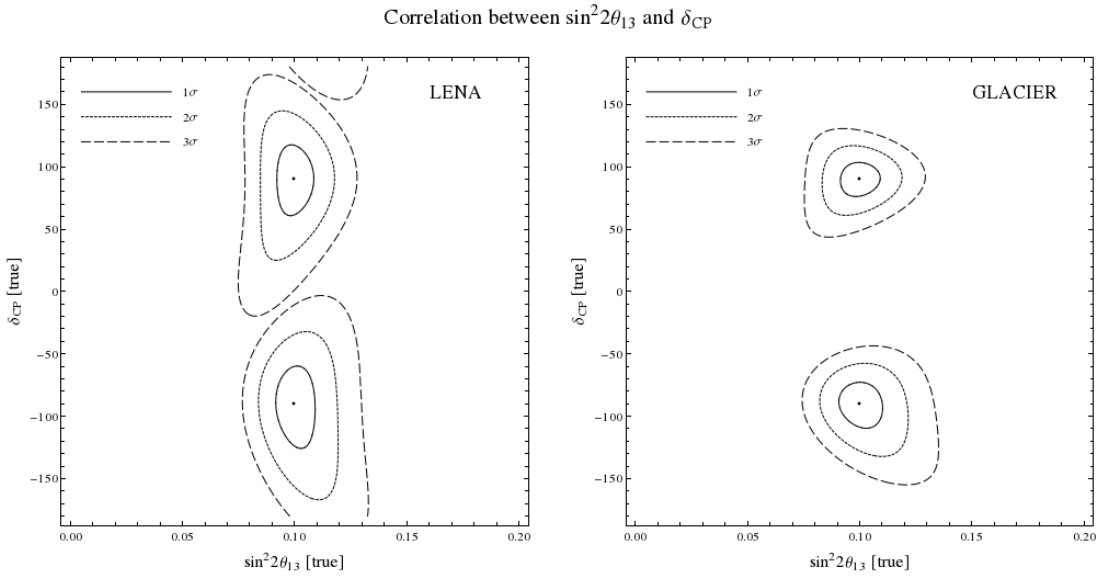

Figure 9: Simulated sensitivities at different $\sin^2 2\theta_{13}$ and δ_{CP} test values when the true values are assumed to be $\sin^2 2\theta_{13} = 0.1$ and $\delta_{\mathrm{CP}} = \pm 90°$.

The graphs in Fig. 9 present the results that would come out from LENA and GLACIER experiments with the given oscillation parameters. The figures show the $1\,\sigma$, $2\,\sigma$ and $3\,\sigma$ contours for the χ^2 distributions, which were computed for LENA and GLACIER setups without parameter correlations assuming only systematic errors. The results show clearly that the larger LArTPC detector GLACIER yields better accuracies for determining the true values of $\sin^2 2\theta_{13}$ and δ_{CP} than the liquid scintillator detector LENA. The allowed-value graphs are similar for other δ_{CP} values, only that the central points move on the $\sin^2 2\theta_{13} - \delta_{\mathrm{CP}}$ plane when the true values are changed, the confidence contours maintaining their shape [42].

The expected accuracy of the measurement of $\sin^2 2\theta_{13}$ can be estimated by taking a projection onto the $\sin^2 2\theta_{13}$ axis. This is carried out by varying only $\sin^2 2\theta_{13}$ in test values and calculating χ^2 for each point. This method is substantially faster than computing the full correlation plot and provides a useful tool for calculating sensitivities for single parameters.

Let us compute a projection by calculating χ^2 first with only systematics and then including parameter correlations. For the correlations, the χ^2 function is minimized in respect to every oscillation parameter except θ_{13}, which is kept fixed. The projected χ^2 distributions are presented in Fig. 10. The true values given in Tab. 5 were used, and the CP violation was kept maximal at $\delta_{\mathrm{CP}} = 90^\circ$ with no constraints assumed, i.e. no priors were used.

From these plots one can now read the sensitivity of LENA and GLACIER experiments on the quantity $\sin^2 2\theta_{13}$ during their proposed 5+5 year running time. Fig. 10 shows the $3\,\sigma$ limits projected onto the $\sin^2 2\theta_{13}$ axis with arrows (thin curves) and shaded areas (thick curves). The setting leads to a situation where LENA roughly measures $\sin^2 2\theta_{13}$ with the accuracy $\sin^2 2\theta_{13} \approx 0.10 \pm 0.04$ at $3\,\sigma$ and GLACIER with the accuracy $\sin^2 2\theta_{13} \approx 0.10 \pm 0.02$, when only systematic errors are taken into account. When one includes the parameter correlations LENA would see no effect, while GLACIER sees it with accuracy $\sin^2 2\theta_{13} \approx 0.10 \pm 0.03$.

The $\sin^2 2\theta_{13}$ projection plots in Fig. 10 also show the simple topology that χ^2 distributions have in the case of superbeam experiments; as the graphs at this range resemble parables with no more than one global minimum, the local minimizers should have no trouble locating it. The situation is different in the case of neutrino factories, for instance, where the χ^2 distribution has evidently more complex topology and at least one additional local minimum [13].

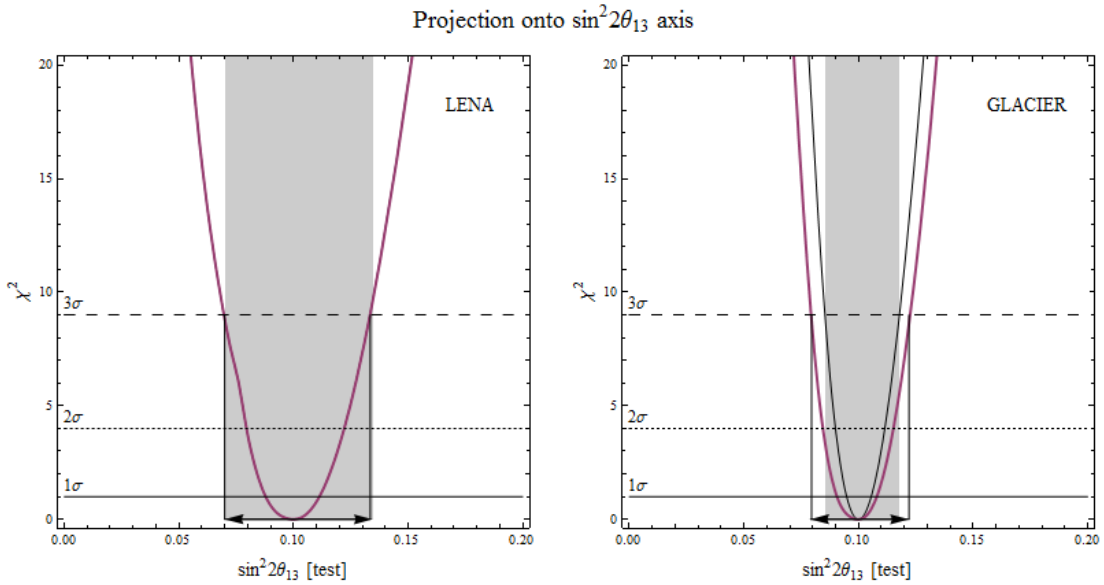

Figure 10: Projection of $\sin^2 2\theta_{13}$ axis for LENA (left panel) and GLACIER (right panel) using the CN2PY beam and assuming $\delta_{CP} = 90°$. Thin curves correspond to the situation where systematics are on and correlations off, and thick curves the situation systematics on, correlations on.

6.3 Non-zero θ_{13}

Another good way to demonstrate the potential of the χ^2 computing engine is to test the sensitivity to confirm the $\theta_{13} > 0$ result in a long baseline neutrino experiment and show how much the result improves from the reactor data. The importance of having a non-zero mixing angle has been established as a vital prerequisite for probing CP violation, which can be seen in the matter-enhanced transition probability formula, where δ_{CP} appears only together with $\sin^2 2\theta_{13}$. This result has been previously obtained in the reactor experiments, but in this section we use GLoBES to simulate how the sensitivity to $\theta_{13} > 0$ would improve if it was tested in the CN2PY experiments.

We use the following strategy to demonstrate the θ_{13} discovery potential with GLoBES. The event rates are computed for the true and test values of which the first is computed from the current best fit oscillation parameter values and the other is set to the corresponding $\theta_{13} = 0$ solution that one wants to rule out. The sensitivity is demonstrated by computing the χ^2 function for different $\sin^2 2\theta_{13}$ and δ_{CP} parameter values. For each graphical point, the corresponding ($\sin^2 2\theta_{13}$, δ_{CP}) values are selected for the oscillation parameters and the other parameter values are taken from Tab. 5. The χ^2 values are calculated

with Eq. (16) keeping all oscillation parameters except θ_{13} free in the minimization process, with θ_{13} fixed to zero. The resulting $\Delta\chi^2 := \chi^2 - \chi^2_{\text{min}}$ distribution is determined from the computed χ^2 value and its smallest value χ^2_{min}, and it gives the confidence level as $\sqrt{\Delta\chi^2} \cdot \sigma$. When the function reaches sufficiently high values, the data is sufficient to rule out the incorrect $\theta_{13} = 0$ solution. We call this quantity as the θ_{13} discovery potential.

We have simulated the θ_{13} discovery potential using the LENA and GLACIER detector setups with the CN2PY beam as described in Ch. 2 and Ch. 3. The simulation was executed by calculating the χ^2 values over the parameter range $\sin^2 2\theta_{13} = 10^{-3}, \ldots, 10^{-1}$ using a logarithmic scale. The CP violation parameter was similarly allowed to go through the values $\delta_{\text{CP}} = -180°, \ldots, 180°$. In this range the χ^2 function has its smallest value $\chi^2_{\text{min}} \approx 0$, and therefore $\Delta\chi^2 \approx \chi^2$. The distributions were calculated assuming first normal hierarchy to be the true hierarchy and then inverted hierarchy was switched to its place. The $5\,\sigma$ confidence level can be shown by plotting the $\chi^2 = 25$ contour for both distributions. We plotted these contours on separate simulations and placed the results together in Fig. 11 and Fig. 12.

In principle, one does not have to know which hierarchy is the correct one in the first place. When the hierarchy is unknown, a fairly good estimate of the discovery potential can be obtained by taking a minimum of χ^2 values at each graphic point. In the case of Fig. 11 and Fig. 12 the minimum $5\,\sigma$ limit corresponds to the IH plot.

The $5\,\sigma$ contours in Fig. 11 show that the sensitivity for $\theta_{13} > 0$ in LENA is slightly better when the correct mass hierarchy is normal hierarchy. The sensitivity is reduced slightly when the simulation is done using inverted hierarchy in true values. This change is mostly due to the slightly smaller absolute value of Δm^2_{31} that has been measured for possible inverted hierarchy solution (cf. Tab. 5). This inaccuracy is relatively small, though, and the $\theta_{13} = 0$ chance can be ruled out with approximately $5\,\sigma$ C.L. almost anywhere in the $\sin^2 2\theta_{13} \gtrsim 0.01$ region. The measurements are favourable in the upper halfplane and unfavourable in the lower since with this choice of mass hierarchy. The $\theta_{13} > 0$ sensitivity becomes particularly huge close to the measured true value region $\sin^2 2\theta_{13} \approx 10^{-1}$, where the confidence level nears as high as $25\,\sigma$ values. This estimation would be a great improvement to the reactor data which confirmed the result recently at roughly $5\,\sigma$.

The sensitivity for θ_{13} discovery potential was also simulated for GLACIER setup, for which the corresponding $5\,\sigma$ contours are given in Fig. 12. The difference between LENA and GLACIER detectors appears in this case as a general shift to the left in the sensitivity plots, which corresponds to approximately

factor 5 improvement to the LENA results.

6.4 Mass hierarchy

Within the framework of the standard three-flavour oscillation theory it is possible to estimate the ability of neutrino experiments to solve the mass hierarchy. We use GLoBES to simulate the events for LENA and GLACIER to test the ability of these experiments to rule out the wrong mass hierarchy of neutrinos, that is, the sign of $\Delta m^2_{31} = m^2_3 - m^2_1$. Similarly to the θ_{13} simulation, we do the mass hierarchy test by computing event rates for each pair of θ_{13} and δ_{CP} values and comparing the results of the normal and inverted hierarchy cases with the χ^2 goodness-of-fit method. If the computed $\Delta\chi^2$ values are large enough, the simulated neutrino experiment can be expected to be capable to rule out the tested hierarchy solution at the given confidence level. This simulation example shows the potential of detecting right mass hierarchy with the experiments.

The mass hierarchy discovery potential is determined much in the same way

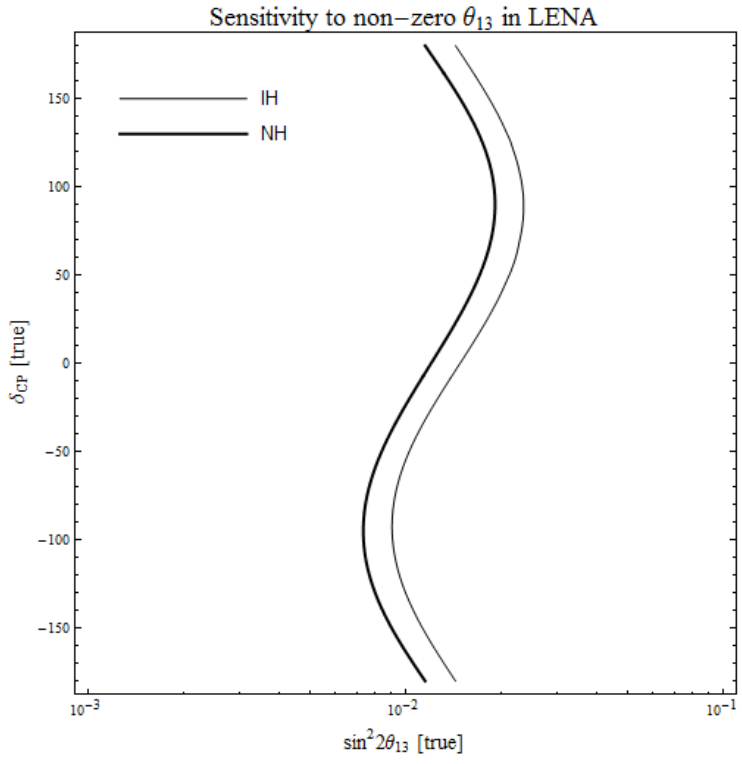

Figure 11: The θ_{13} discovery potential at LENA with $5\,\sigma$ confidence level illustrated. Both normal and inverted hierarchy solutions are shown.

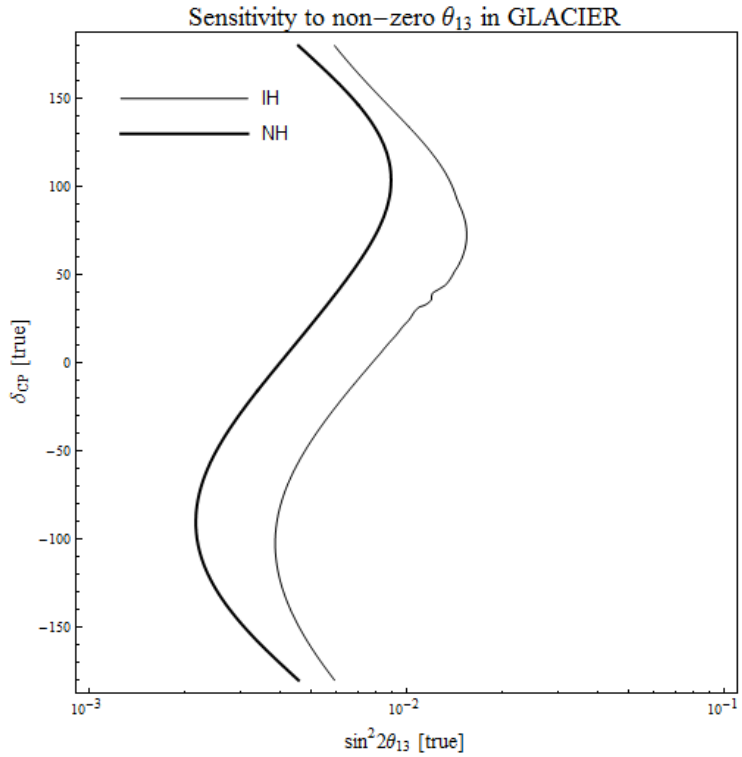

Figure 12: The θ_{13} discovery potential at GLACIER with $5\,\sigma$ confidence level illustrated. Both normal and inverted hierarchy solutions are shown.

as the θ_{13} discovery potential, described in Sec. 6.3. The simulator computes the event rates for each $(\sin^2 2\theta_{13}, \delta_{\rm CP})$ point with true values ω_0 and test values ω where both are assigned different mass hierarchies. The corresponding χ^2 values are then computed for both the two hierarchies keeping Δm^2_{31} fixed and other parameters free. The compatibility between the test and true mass hierarchy alternative is then given by a $\Delta\chi^2$ distribution, which is computed as subtraction of the χ^2 values, i.e. $\Delta\chi^2 := \chi^2(\text{test hierarchy}) - \chi^2(\text{true hierarchy})$ shows the confidence level at which the test hierarchy can be rejected as false solution on basis of the simulated data.

The true and test hierarchies are not to be confused with the oscillation parameter sets that are conventionally referred in this paper as true and test values. Since the task here is to compare the data sets corresponding to two discrete hierarchy values, the χ^2 function has to be minimized for both the normal and inverted cases with respect to test values. The hierarchy inversion is carried out via the conversion $\Delta m^2_{31} \rightarrow -\Delta m^2_{21} + \Delta m^2_{31}$ of the true value Δm^2_{31}, which in turn is set manually at the beginning of the simulation process. The $\chi^2_{\rm total}$ function given in Eq. (16) is evaluated by using first normal and then

inverted hierarchies in test values, and the difference is presented as the final $\Delta\chi^2$, which indicates the statistical difference between the test hierarchy and true hierarchy data.

The simulation script was first set to test inverted hierarchy against normal hierarchy with $\Delta\chi^2 = \chi^2(\text{IH}) - \chi^2(\text{NH})$ and then other way round, i.e. $\Delta\chi^2 = \chi^2(\text{NH}) - \chi^2(\text{IH})$. The oscillation parameters were defined as in Tab. 5 and varying $\sin^2 2\theta_{13}$ and δ_{CP} through values $10^{-3}, \ldots, 10^{-1}$ and $-180°, \ldots, 180°$, respectively. The results were plotted as $3\,\sigma$ contours by setting $\Delta\chi^2 = 9$ (see Fig. 13 and Fig. 14).

In the first run we used the normal hierarchy value $\Delta m^2_{31} = 2.45 \times 10^{-3}\text{eV}^2$ in the true values (true hierarchy NH) and switched it to $\Delta m^2_{31} = -2.34 \times 10^{-3}\text{eV}^2$ for inverted hierarchy (true hierarchy IH), which correspond to the best-fit values of Tab. 5. The test hierarchy was chosen similarly as the opposite hierarchy, leaving a setup that shows the $\sin^2 2\theta_{13}$ and δ_{CP} values of which the test hierarchy can be distinguished from true hierarchy by $3\,\sigma$ margin. The plot in the case of LENA is presented in Fig. 13.

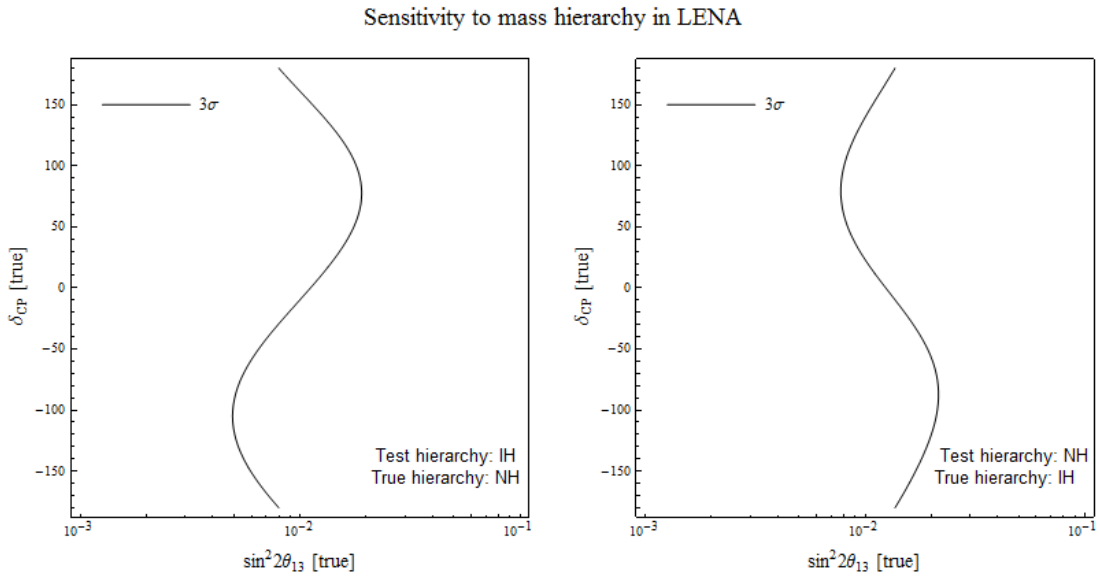

Figure 13: The sensitivity of the LENA experiment for the mass hierarchy discovery. The line indicates the region in the parameter space where the test hierarchy can be ruled out at $3\,\sigma$ C.L. Higher confidence levels are achieved towards the right.

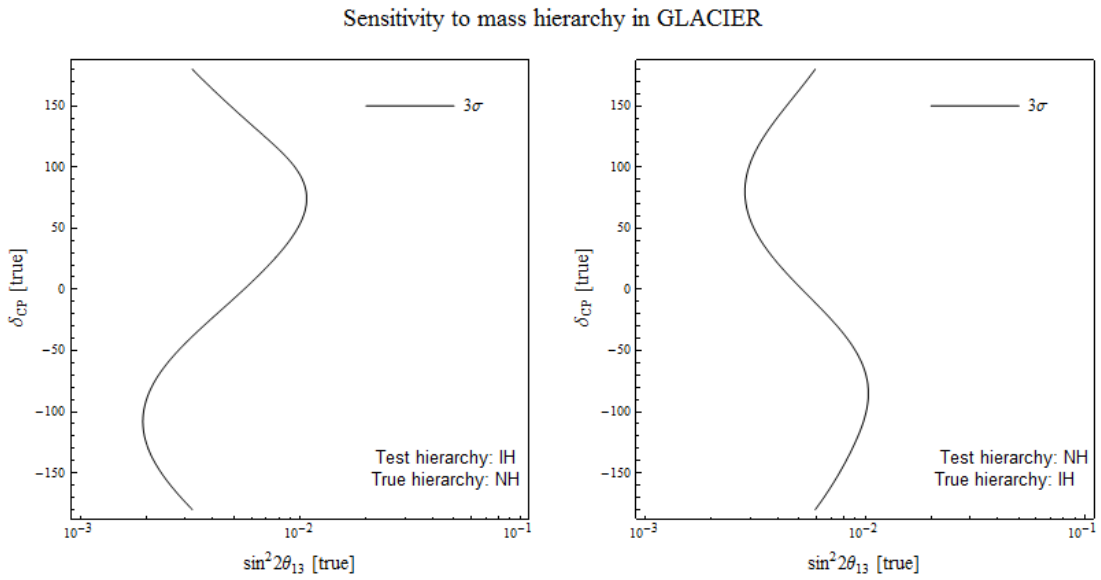

Figure 14: The sensitivity of the GLACIER experiment for the mass hierarchy discovery. The line indicates the region in the parameter space where the test hierarchy can be ruled out at $3\,\sigma$ C.L. Higher confidence levels are achieved towards the right.

The left panel in Fig. 13 tests the inverted hierarchy against the normal hierarchy. The $\Delta\chi^2$ distribution is a smooth function which gets its lowest values near to $\sin^2 2\theta_{13} = 0$, the values of $\sin^2 2\theta_{13}$ increasing towards the right end of the frame. The region left to the $3\,\sigma$ contour shows the parameter values at which the simulated data is inconclusive and can not distinguish the wrong-sign hierarchy from the right-sign hierarchy. In this region $\Delta\chi^2 < 9$, and the mass hierarchy discovery sensitivity falls short from the $3\,\sigma$ limit. The region to the right, on the contrary, shows the parameter values for which the mass hierarchy problem can be solved.

The right panel in Fig. 13 gives the $3\,\sigma$ limit for rejecting the normal hierarchy. The shape of the graph has much in common with the one in the left panel, but the inversion of the studied hierarchies turns the curve into a reflection from the previous case. The slightly smaller absolute value of the inverted hierarchy mass (current best-fit from previous experiments) also pushes the curve to the right, reducing the sensitivity systematically. In general, the best results for mass hierarchy discovery sensitivity is received near $\delta_{\mathrm{CP}} \sim -110°$ and the worst near $\delta_{\mathrm{CP}} \sim 80°$ for the inverted hierarchy case. The CP phase values are correspondingly switched when the test hierarchy is changed to normal hierarchy with some variation of the peak values. The δ_{CP} values can therefore be

classified into half-planes, in which the mass hierarchy search can be favoured or disfavoured.

The difference between LENA and GLACIER performances again proves to be very significant. The liquid argon time projection chamber setup leads to $3\,\sigma$ C.L. contours that are of the same shape as those of the liquid scintillator, but generally by a factor of 5 better (see Fig. 14). In the end, the signal for mass hierarchy discovery can be expected to be confirmed at approximately $\sin^2 2\theta_{13} > 0.02$ range for all δ_{CP} values in LENA and $\sin^2 2\theta_{13} > 0.01$ in GLACIER. This estimation is very rough and most likely slightly optimistic. Since the current best-fit value is $\sin^2 2\theta_{13} \approx 0.1$, the mass hierarchy question can be answered at any δ_{CP} value.

There is one major shortcoming in the method we have used in this section for the determination of the mass hierarchy. The statistical analysis described above relies on the fundamental assumption that the computed $\Delta\chi^2$ distribution is a χ^2 distribution with one degree of freedom due to the so called Wilks's theorem [57]. While this is generally true for χ^2 distributions that involve continuous quantities, such as allowed parameter ranges and non-zero θ_{13}, the mass hierarchy problem studies two discrete values, to which the theorem does not apply [58, 59]. In absence of better statistical methods, however, the conventional confidence level estimator provides a fair approximation for the mass hierarchy discovery potential, and the results presented in this study can be used as preliminary results.

6.5 CP violation

One of the key motivations for the neutrino oscillation research has been the possible determination of the leptonic CP phase parameter δ_{CP}. Given the relatively large value of the mixing angle θ_{13}, as revealed by Daya Bay and other reactor neutrino experiments, this is a realistic goal of the next generation neutrino experiments. In this section we consider a simulation that probes the experiment's ability to search for the signs of CP violation. We conduct this study by using the GLoBES software to compute the event rates for a range of ($\sin^2 2\theta_{13}$, δ_{CP}) points and compare them with another set of data that follows from the CP conserving solutions $\delta_{\mathrm{CP}} = 0, \pi$. The outcome is a $\Delta\chi^2$ which determines the chance at which the CP conserving solution can be dismissed.

The analysis is done with the same strategy that was employed in θ_{13} and mass hierarchy discovery cases in Sec. 6.3 and 6.4. The $\Delta\chi^2$ distribution is computed from Eq. (16) as $\Delta\chi^2 = \chi^2 - \chi^2_{\mathrm{min}}$ by taking into account systematics and parameter correlations. The minimization process is executed for

every parameter, excluding δ_{CP}, which is kept fixed. We also keep the mass squared difference Δm^2_{31} fixed to its best-fit values, first $2.45 \times 10^{-3}\,\mathrm{eV}^2$ for NH and $-2.34 \times 10^{-3}\,\mathrm{eV}^2$ for IH [16], to account the mass hierarchy. At each data point, the χ^2 value is calculated assembling the true value vector ω_0 from the corresponding ($\sin^2 2\theta_{13}$, δ_{CP}) values accompanied with the generic information given in Tab. 5. The test values ω are the same as the true values ω_0, except the CP phase is set first to $\delta_{CP} = 0$ and then $\delta_{CP} = \pi$, i.e. the CP conserving values. The χ^2 function is evaluated through the parameter range $\sin^2 2\theta_{13} = 0.01, \ldots, 0.1$ and $\delta_{CP} = -180°, \ldots, 180°$. At this range the minimum value of χ^2 becomes zero and $\Delta\chi^2 = \chi^2$.

Let us first search for CP violation recalling that the mass hierarchy problem is not yet determined. We first simulate the CP violation discovery potential by calculating $\Delta\chi^2$ with Δm^2_{31} kept fixed to its NH value $2.45 \times 10^{-3}\mathrm{eV}^2$ and δ_{CP} fixed to the corresponding graphic point. The simulation was run using GLoBES for the LENA experiment whose specifications were given in Ch. 5. The computation was then repeated with Δm^2_{31} fixed to the IH value $\Delta m^2_{31} = -2.34 \times 10^{-3}\mathrm{eV}^2$. The resulting sensitivity plots are presented in Fig. 15. The $3\,\sigma$ contours correspond to $\Delta\chi^2 = 9$. LENA does not appear to have $3\,\sigma$ sensitivity, so we have plotted $1.5\,\sigma$, $2.0\,\sigma$ and $2.5\,\sigma$ contours instead. The results of a similar analysis for the GLACIER experiment are presented in Fig. 16, where $2.5\,\sigma$, $3.0\,\sigma$ and $3.5\,\sigma$ contours are plotted for illustration.

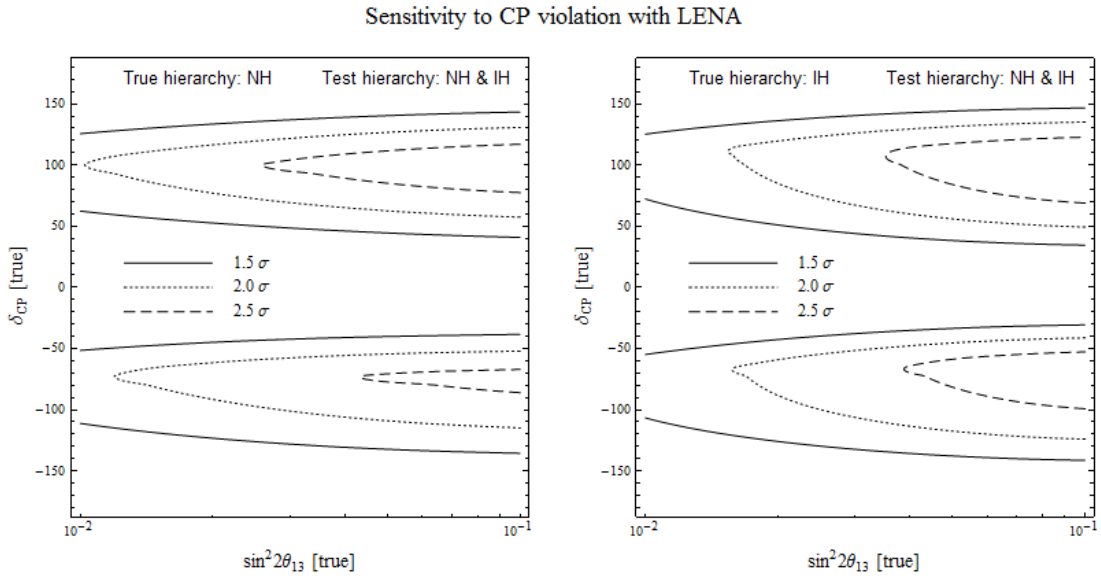

Figure 15: The 1.5, 2.0 and $2.5\,\sigma$ sensitivity plots for CP violation discovery in the LENA detector.

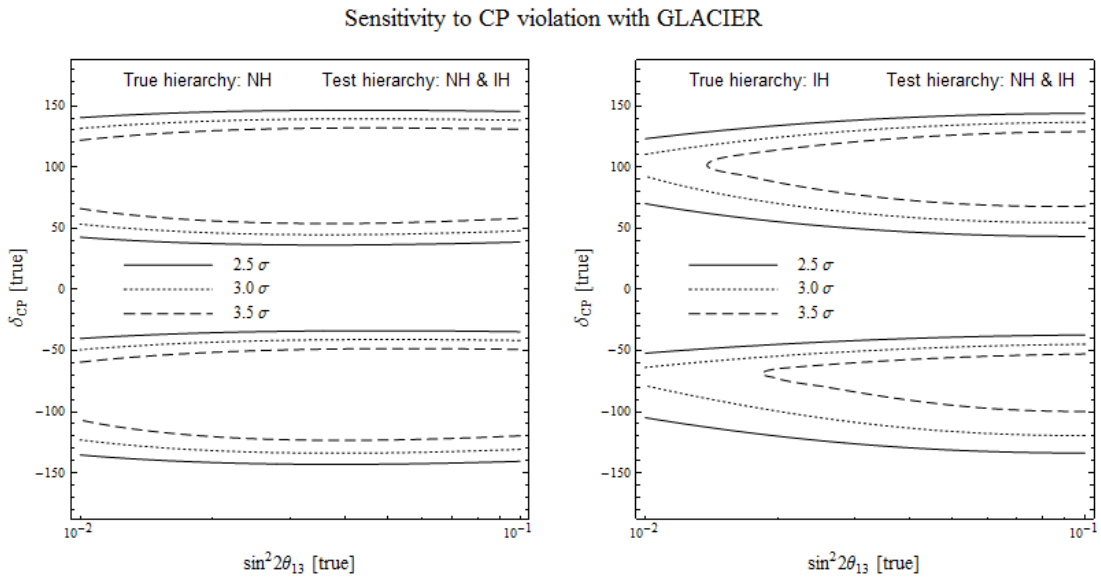

Figure 16: The 2.0, 2.5 and 3.5 σ sensitivity plots for CP violation discovery in the GLACIER detector.

The plots presented in Figs. 15 and 16 show the CP violation discovery potential of LENA and GLACIER assuming the high-intensity HP-PS2 beam and 5+5 years running time. The $\Delta\chi^2$ contours appear as a pair of regions where $\Delta\chi^2 \geq 9$. In these regions the CP conservation is eliminated with $3\,\sigma$ confidence. Outside these regions $\Delta\chi^2 \leq 9$ and the effect of possible CP violation can not be distinguished on the basis of data. The shapes of the graphs are nearly identical in both mass hierarchy cases, which suggests that the sensitivity for CP violation does not have any strong correlation to mass hierarchy in this parameter range.

From Fig. 15 one can read that for the experimentally obtained value $\sin^2 2\theta_{13} \approx 0.1$ the LENA detector will cover about 17% in the case of normal hierarchy and about 25% in the case of inverted hierarchy of the values of $\delta_{\mathrm{CP}} = -180°, \ldots, 180°$ with $2.5\,\sigma$ sensitivity. From Fig. 16 one can infer that GLACIER yields roughly 61% for normal hierarchy and 56% for inverted hierarchy. This δ_{CP} coverage is reduced to 44% and 42% for GLACIER when the required confidence level is $3\,\sigma$. LENA has no $3\,\sigma$ sensitivity at $\sin^2 2\theta_{13} = 0.1$.

6.6 Octant degeneracy and θ_{23}

The final example of parameter degeneracy that we consider concerns the mixing angle θ_{23}, which is usually determined from atmospheric data. Recent studies have provided a relatively good estimate for the value of this parameter, but the precise determination has been hindered by the so called octant degeneracy, that is, θ_{23} and $90° - \theta_{23}$ lead to the same values of observables. The true θ_{23} is known to be either slightly over or alternatively under the conventional value $\theta_{23} = 45°$. In this section we determine the values of θ_{23} for which the mixing angle can be determined free of the (θ_{23}, $90° - \theta_{23}$) degeneracy. The simulation is run with LENA and GLACIER setups to determine which $\Delta\chi^2 = \chi^2 - \chi^2_{\text{min}}$ values can be reached with the CN2PY beamline.

The strategy is the same that we applied on computing sensitivities for the mass hierarchy discovery. During the course of simulation, we vary θ_{23} around its conventional central value 45° and force the minimizers to the wrong-sign solution $90° - \theta_{23}$. The resulting χ^2 value then shows the confidence level at which the $90° - \theta_{23}$ value can be ruled out. The test and true value vectors ω and ω_0 are determined at each graphical point ($\sin^2 2\theta_{13}$, $\theta_{23} - 45°$) such that θ_{12}, Δm^2_{21}, Δm^2_{31} and $\hat{\rho}$ correspond to the experimentally confirmed values given in Tab. 5 and the test values are obtained through the switch $\theta_{23} \to 90° - \theta_{23}$. The χ^2 value is computed with Eq. (16) by testing $90° - \theta_{23}$ against θ_{23} at every graphical point, keeping every parameter except θ_{23} free in the minimization process. We also assume maximum CP violation and set $\delta_{\text{CP}} = 90°$. We simulate $\theta_{23} - 45°$ as a function of $\sin^2 2\theta_{13}$ which is varied through $10^{-3}, \ldots, 10^{-1}$, and show the $3\,\sigma$ limits for both normal and inverted hierarchy cases by setting $\Delta\chi^2 = 9$ contours. With this setup, the smallest χ^2 value is zero, and we have $\Delta\chi^2 = \chi^2$.

Let us first consider the ability to solve the (θ_{23}, $90° - \theta_{23}$) degeneracy using LENA. The results of the simulations are presented in the left panel of Fig. 17, where the $3\,\sigma$ confidence contours are given. According to the simulation results, the LENA experiment is expected to measure $3\,\sigma$ or better sensitivity at $\sin^2 2\theta_{13} \approx 0.1$ only if θ_{23} differs by 3° or more from 45° and normal hierarchy is assumed. The sensitivity is worse for the inverted hierarchy case. Similarly GLACIER can be expected to solve the (θ_{23}, $90° - \theta_{23}$) degeneracy at $3\,\sigma$ C.L. if the difference is more than 2.5° and normal hierarchy is assumed (see the right panel of Fig. 17).

Fig. 17 shows that the sensitivity to solve the (θ_{23}, $90° - \theta_{23}$) degeneracy depends strongly on the mass hierarchy and the exact value of $\sin^2 2\theta_{13}$. We also repeated the simulation for different values of δ_{CP}, but the results were approximately the same as with maximum CP violation.

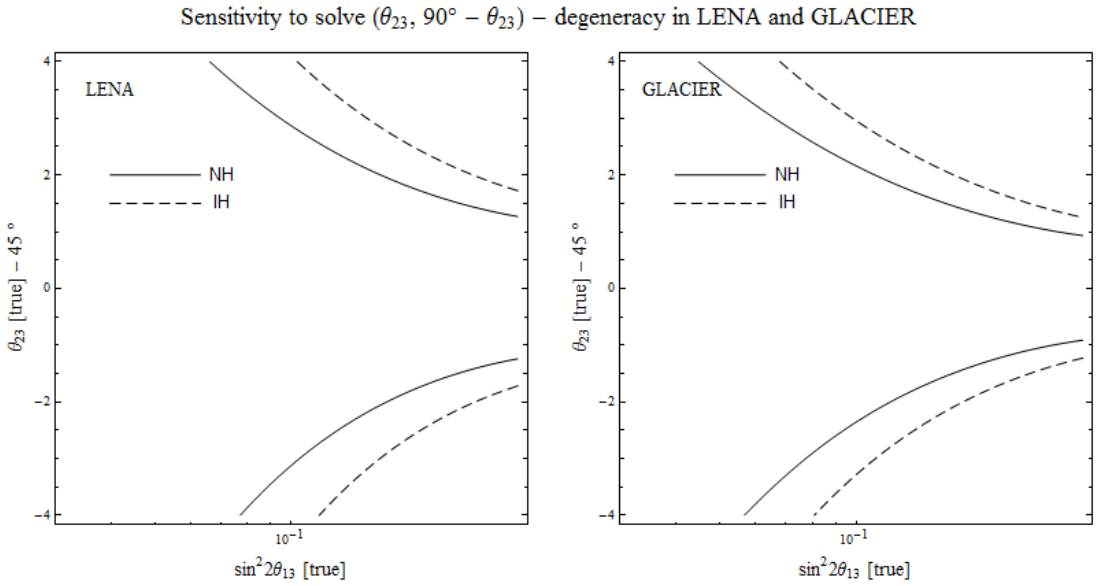

Figure 17: The $3\,\sigma$ sensitivity plots for θ_{23} discovery at both normal and inverted hierarchy. The region between the lines mark the θ_{23} values at which the two degenerate solutions become indistinguishable.

6.7 Impact of systematics and NC background

In previous sections we have considered experiment parameters that are not very well known as the technology for their more exact determination is still under development. The simulation of the future experiments requires accurate information on subjects like systematic errors, detection efficiencies and background contribution, and they should be updated as soon as detailed information about the technology is available. Here we try to estimate the effect of systematic errors and background events by simulating the mass hierarchy sensitivity for LENA by varying the corresponding weight parameters.

The first parameters to consider are the weight factors of systematic errors, which were given in Eq. (13). In Sec. 6.4 we described the systematics as energy normalization and event rate calibration errors, scaled with parameters π_a, π_b and π_c, π_d. To make comparisons between different values of systematic errors we have recalculated the $\Delta\chi^2$ values with doubled weight values and plotted the resulting $3\,\sigma$ contour to the same figure (see the left panel of Fig. 18). We have similarly computed the $\Delta\chi^2$ values for the doubled NC acceptance rate to test how much the NC background changes the final mass hierarchy sensitivity in muon disappearance channels (see the right panel of Fig. 18).

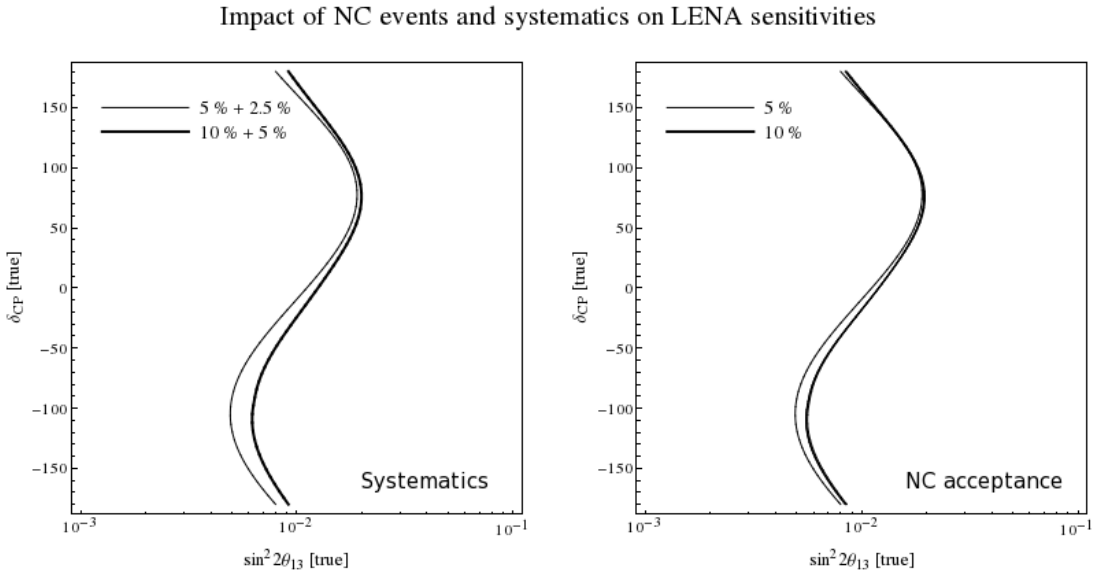

Figure 18: The impact of systematics and NC on LENA sensitivity.

The results show that doubling the error margins in systematics or NC background shifts the 3σ lines slightly. The results prove that the impact of the energy normalization and calibration errors are rather small in the final sensitivity to mass hierarchy. Neither does the relative weight of NC background affect the mass hierarchy measurement.

7 Conclusions

We have studied in this work the prospects for determining in a long baseline neutrino oscillation experiment with a high-powered superbeam the values of the central neutrino mixing parameters like the neutrino mass hierarchy (the sign of Δm^2_{31}) and the leptonic CP violation angle $\delta_{\rm CP}$. We have paid particular interest in the proposed HP-PS2 synchrotron facility, which has been designed to provide energetic muon neutrinos at an unprecedented intensity. The technology is planned to deliver neutrino energies at multi-GeV scale with intensity of 2 MW. We have studied the details of two next-generation large scale neutrino detectors, one using the liquid scintillator method (LENA) and another using the liquid argon method (GLACIER). Both facilities could be used to study neutrino oscillations with a single detector by comparing information from $\nu_\mu \to \nu_e$ and $\nu_\mu \to \nu_\mu$ channels and corresponding antineutrino channels.

If approved, the superbeam experiment will also be used to study CP violation and improve the determination of other oscillation parameters.

We have tested the detection capabilities of LENA and GLACIER with the 2288-km-long baseline CERN to Pyhäsalmi, assuming the beam properties that were announced in the HP-PS2 design study [24]. The experiment setups were simulated with the GLoBES simulation code, which computed the χ^2 goodness-of-fit test by comparing simulated event rates in different scenarios. The simulated event rates show remarkable signal-to-background ratio for both facilities for electron appearance channels $\nu_\mu \rightarrow \nu_e$ in the proximity to the first oscillation maximum at 4.7 GeV with the default oscillation parameter values used by the software (see Sec. 6.1). The simulated rates also show a clear sign of a second oscillation maximum, which is unavailable in the present experiments. The second oscillation maximum could provide access to study e.g. non-standard interactions [42, 60].

We used the χ^2 feature of GLoBES to compute the correlation between $\sin^2 2\theta_{13}$ and δ_{CP} allowing both parameters have different values, (see Sec. 6.2). The results showed significantly improved sensitivities for all values of $\sin^2 2\theta_{13}$ and δ_{CP}, estimating $\sin^2 2\theta_{13} \approx 0.10 \pm 0.04$ for 5+5 years of LENA and $\sin^2 2\theta_{13} \approx 0.10 \pm 0.03$ for GLACIER measurements. These results were obtained for $3\,\sigma$ confidence level when the true values of $\sin^2 2\theta_{13}$ and δ_{CP} were taken to be 0.1 and 90°, respectively. The correlation between $\sin^2 2\theta_{13}$ and δ_{CP} is strong, and any measurement on one parameter depends on the value of the other. We also tested the simulator by studying how LENA and GLACIER would perform at showing the $\theta_{13} > 0$ result, which had previously been confirmed in reactor experiments (see Sec. 6.3). We found the reactor experiment sensitivity ($\sim 5\,\sigma$ C.L.) rise to near $25\,\sigma$ values around the current best-fit value $\sin^2 2\theta_{13} \approx 0.1$, seeing better results in GLACIER performance when compared to that of LENA.

The determination of the mass hierarchy has been found feasible for both LENA and GLACIER setups with the high-intensity HP-PS2 beam, as shown in Sec. 6.4. We found that the smallest value for $\sin^2 2\theta_{13}$ to identify the correct mass hierarchy at $3\,\sigma$ C.L. was $\sin^2 2\theta_{13} \sim 0.01$ for LENA, depending on the true value of mass hierarchy. In this case the correlation with δ_{CP} is also strong, and the sensitivity to solve mass hierarchy is favoured in lower (upper) δ_{CP} half-plane when NH (IH) is true hierarchy. This sensitivity rises to $4\,\sigma - 5\,\sigma$ confidence levels near the best-fit value $\sin^2 2\theta_{13} \approx 0.1$, implying that the correct mass hierarchy can be determined with LENA in all cases with high confidence. For GLACIER, the results show an improvement of approximately factor 5 for the $3\,\sigma$ C.L. compared with the LENA results.

The search for positive CP violation signals was done by looking for the parameter values, where the CP conserving values $\delta_{CP} = 0, \pi$ could be ruled out (see Sec. 6.5). We studied the performance of LENA and GLACIER assuming that the mass hierarchy is not known. The results of LENA cover approximately 17% (25%) of all δ_{CP} values at the best-fit value $\sin^2 2\theta_{13} \approx 0.1$ when NH (IH) is used as true hierarchy. The result was obtained by computing the $2.5\,\sigma$ C.L. limit. As such, LENA does not turn up much sensitivity at confirming the presence of CP violation, and the simulated data showed no sensitivity at all with $3\,\sigma$ contours. The GLACIER setup outperforms LENA in this case, providing 61% and 56% sensitivities for NH and IH at $2.5\,\sigma$. According to the simulated data GLACIER can also signal positive CP violation at $3\,\sigma$ C.L. with 44% and 42% for NH and IH solutions, respectively. The results evidently improve when the mass hierarchy is identified [30, 42].

The simulation work was completed with a review on the $(\theta_{23}, 90° - \theta_{23})$ hierarchy (see Sec. 6.6). We simulated the sensitivity to rule out the degenerate $90° - \theta_{23}$ solution assuming different values for θ_{23}. The $3\,\sigma$ C.L. limit was reached when the mixing angle was approximately 3° or more off from 45° in the case of LENA and 2.5° in the case of GLACIER. The computed sensitivities of LENA and GLACIER would therefore be not powerful enough to solve the $(\theta_{23}, 90° - \theta_{23})$ degeneracy at $3\,\sigma$ for the current best-fit value $\theta_{23} \approx 45.6°$ [15].

The simulation results show a clear difference between the sensitivities of the two proposed detector alternatives LENA and GLACIER in every measurement task, favouring GLACIER due to its larger detector size and the more delicate detection technology. The general trend shows very good sensitivities for the mass hierarchy determination despite the background events coming from misidentified NC events and the intrinsic beam background. Our simulations show, however, that the effects of these two factors are small to the sensitivities for mass hierarchy (see Sec. 6.7). Other studies have shown that the NC background is more important in the case of CP violation measurements [30]. The results obtained here are also in agreement with the recent simulation studies (see [42, 46] for examples), though some variation occurs as a result to differently chosen simulation parameters. The choice of parameters we made in the simulations are based on earlier studies that use GLoBES [16, 28, 29, 42, 46, 61, 62, 63].

The HP-PS2, LENA and GLACIER development studies are still on an early stage, and not much accurate information has been made available for elements concerning parameters like systematic errors, NC event rejection, energy dependent efficiencies etc. In this light the results in LENA and GLACIER can be found very much sufficient when one takes into account the uncertainty

that arises form considered systematics, beam composition, neutrino cross sections and other elements that require further study. The simulation model we used in this paper is found to be rather simplistic for describing fully the delicate processes of event detection and reconstruction, especially in LArTPC systems. The χ^2 method has also its problems in the mass hierarchy study. The computed χ^2 values presented in this study should therefore be considered as precursory results that show the direction at early stage studies. The simulations can be made more realistic e.g. by implementing more accurate information from oscillation parameters, neutrino interactions [64], cross sections [65, 66], systematics [54] and introducing migration matrices [55]. More sophisticated methods for the statistical analysis of the mass hierarchy data have recently been discussed in [45].

References

[1] C. Giunti and C. W. Kim, *Fundamentals of Neutrino Physics and Astrophysics*, Oxford University Press, NY, USA, 2007

[2] V. Barger, D. Marfatia and K. Wishnant, *The Physics of Neutrinos*, Princeton University Press, NJ, USA, 2012

[3] G.J. Feldman, J. Hartnell and T. Kobayashi, *A Review of Long-baseline Neutrino Oscillation Experiments* (2013), arXiv:1210.1778

[4] G.L. Fogli *et al.*, *Global analysis of neutrino masses, mixings and phases: entering the era of leptonic CP violation searches* (2012), arXiv:1205.5254v1

[5] P. Coloma, A. Donini, E. Fernández-Martínez and P. Hernández, *Precision on leptonic mixing parameters at future neutrino oscillation experiments*, JHEP 06 (2012) 073, arXiv:1203.5651v2

[6] F. An *et al.*, *Improved Measurement of Electron Antineutrino Disappearance at Daya Bay*, Chin. Phys. C37 (2013) 011001, arXiv:1210.6327v2

[7] J. Ahn *et al.*, *Observation of Reactor Electron Antineutrino Disappearance in the RENO Experiment*, Phys.Rev.Lett. 108 (2012) 191802, arXiv:1204.0626v2

[8] Y. Abe *et al.*, *Reactor $\bar{\nu}_e$ disappearance in the Double Chooz experiment*, Phys.Rev. D86 (2012) 052008, arXiv:1207.6632v2

[9] Y. Abe *et al.*, *First Measurement of θ_{13} from Delayed Neutron Capture on Hydrogen in the Double Chooz Experiment* (2013), arXiv:1301.2948v1

[10] A. Habig, *MINOS neutrino oscillation results*, Mod. Phys. Lett. A25, 1219-1231 (2010), arXiv:1004.2647v1

[11] T.K. Abe *et al.*, *Indication of Electron Neutrino Appearance from an Accelerator-produced Off-axis Muon Neutrino Beam*, Phys. Rev. Lett. 107 (2011) 041801, arXiv:1106.2822

[12] P. Huber, M. Lindner and W. Winter, *Simulation of long-baseline neutrino oscillation experiments with GLoBES (General Long Baseline Experiment Simulator)*, Comput. Phys. Commun. 167 (2005) 195, arXiv:hep-ph/0407333

[13] P. Huber, J. Kopp, M. Lindner, M. Rolinec, and W. Winter, *New features in the simulation of neutrino oscillation experiments with GLoBES 3.0*, Comput. Phys. Commun. 177 (2007), p. 432-438, arXiv:hep-ph/0701187

[14] K. Eguchi *et al.*, *A High Sensitivity Search for $\bar{\nu}_e$'s from the Sun and Other Sources at KamLAND*, Phys. Rev. Lett. 92 (2004) 071301, arXiv:hep-ex/0310047v3

[15] R. Wendell *et al.*, *Atmospheric neutrino oscillation analysis with sub-leading effects in Super-Kamiokande I, II, and III*, Phys. Rev. D81 (2010) 092004, arXiv:1002.3471

[16] S. Prakash, S.K. Raut and S.U. Sankar, *Getting the best out of T2K and NOvA*, Phys. Rev. D86 (2012) 033012, arXiV:1201.6485v3

[17] D. Ayres *et al.*, *NOvA Proposal to Build a 30 Kiloton Off-Axis Detector to Study Neutrino Oscillations in the Fermilab NuMI Beamline*, Fermilab-Proposal-0929 (2005), arXiv:hep-ex/0503053v1

[18] T. Akiri *et al.*, *The 2010 Interim Report of the Long-Baseline Neutrino Experiment Collaboration Physics Working Groups* (2011),

arXiv:1110.6249v1

[19] T. Ishida, *T2HK: J-PARC upgrade plan for future and beyond T2K*, KEK Preprint 2013-55 (2013), arXiv:1311.5287v1

[20] T. Patzak *et al.*, *LAGUNA-LBNO: Large Apparatus studying Grand Unification and Neutrino Astrophysics and Long Baseline Neutrino Oscillations*, TAUP 2011, Journal of Physics: Conference series 375 (2012)

[21] A. Rubbia *et al.*, *The LAGUNA design study- towards giant liquid based underground detectors for neutrino physics and astrophysics and proton decay searches*, Acta Physica Polonica B, vol. 41, no. 7 (2010), p. 1727-1732, arXiv:1001.0077v1

[22] M. Wurm *et al.*, *The next-generation liquid-scintillator neutrino observatory LENA*, Astropart. Phys. Vol. 12, Iss. 11 (2013), p. 685-732 arXiv:1104.5620v3

[23] A. Rubbia, *Underground Neutrino Detectors for Particle and Astroparticle Science: the Giant Liquid Argon Charge Imaging ExpeRiment (GLACIER)*, J. Phys. Conf. Ser. 171 (2009) 012020, arXiv:0908.1286v1

[24] R. Steerenberg *et al.*, *CERN High-Power Proton Synchrotron Design Study For LAGUNA-LBNO Neutrino Production*, MOP244, Proc. of HB2012, Beijing, China (2012)

[25] S. Vihonen, *Neutrino oscillations in matter and magic baselines*, Bachelor's Thesis, University of Jyväskylä (2012)

[26] M. Freund, *Analytic approximations for three neutrino oscillation parameters and probabilities in matter*, Phys. Rev. D64 (2001) 053003, arXiv:hep-ph/0103300

[27] S. Vihonen, *Numerical simulation of long baseline neutrino oscillation experiments with GLoBES*, 2nd Bachelor's Thesis, University of Jyväskylä (2013)

[28] V. Barger, P. Huber, D. Marfatia, and W. Winter, *Upgraded experiments with super neutrino beams: Reach versus Exposure*, Phys. Rev.,

D76, 031301 (2007), arXiv:hep-ph/0610301

[29] V. Barger, P. Huber, D. Marfatia and W. Winter, *Which long-baseline neutrino experiments are preferable?*, Phys. Rev. D76, 053005 (2007), DOI:10.1103/PhysRevD.76.053005

[30] P. Coloma, T. Li and S. Pascoli, *Long-baseline super-beam experiments in Europe within LAGUNA*, J. Phys. Conf. Ser. 408 (2013) 012036, doi:10.1088/1742-6596/408/1/012036

[31] S.K. Agarwalla, *Some Aspects of Neutrino Mixing and Oscillations*, Doctoral thesis, University of Calcutta (2009), arXiv:0908.4267v2

[32] J. Peltoniemi, *Simulations of neutrino oscillations for a wide band beam from CERN to LENA* (2009) arXiv:0911.4876v1

[33] G. Alimonti *et al.*, *The Borexino detector at the Laboratori Nazionali del Gran Sasso*, Nucl. Inst. and Meth. A, Vol. 600, Iss. 3, 568-593 (2009), arXiv:0806.2400v1

[34] M.C. Chen, *The SNO+ experiment*, ICHEP2008 (2008), arXiv:0810.3694

[35] N.K. Mondal, *Status of India-based Neutrino Observatory (INO)*, Proc. Indian Natn. Sci. Acad., 70, A, No.1, p.71-77 (2004)

[36] G. S. Karagiorgi, *Current and Future Liquid Argon Neutrino Experiments*, Columbia University (2013), arXiv:1304.2083

[37] F. Arneodo *et al.*, *The ICARUS Experiment, A Second-Generation Proton Decay Experiment and Neutrino Observatory at the Gran Sasso Laboratory*, LNGS-P28/2001 (2001), arXiv:hep-ex/0103008v1

[38] C. Anderson *et al.*, *The ArgoNeuT Detector in the NuMI Low-Energy beam line at Fermilab* JINST 7 (2012) P10019, arXiv:1205.6747

[39] R.J. Wilkes *et al.*, *UNO*, UW/PT 05-21 (2005), arXiv:hep-ex/0507097v1

[40] L. Agostino *et al.*, *Study of the performance of a large scale water-Cherenkov detector (MEMPHYS)*, JCAP 01 (2013) 024,

arXiv:1206.6665

[41] A. Bross *et al.*, *A Toroidal Magnetised Iron Neutrino Detector (MIND) for a Neutrino Factory*, Phys. Rev. ST Accel. Beams 16, 081002 (2013), arXiv:1306.5327v2

[42] P. Coloma, T. Li and S. Pascoli, *A comparative study of long-baseline superbeams within LAGUNA for large θ_{13}* (2012), arXiv:1206.4038v1

[43] N. Agafonova *et al.*, *Search for $\nu_\mu \rightarrow \nu_e$ oscillations with the OPERA experiment in the CNGS beam*, JHEP 07 (2013) 004, arXiv:1303.3953v2

[44] K. Abe *et al.*, *The T2K Neutrino Flux Prediction*, T2K collaboration (2013), arXiv:1211.0469v3

[45] P. Coloma, E. Fernández-Martínez, L. Labarga, *Physics reach of CERN-based SuperBeam neutrino oscillation experiments*, JHEP 1211 (2012) 069, arXiv:1206.0475

[46] S. Agarwalla, T. Li and A. Rubbia, *An incremental approach to unravel the neutrino mass hierarchy and CP violation with a long-baseline Superbeam for large θ_{13}*, JHEP 05 (2012) 154, arXiv:1109.6526

[47] A. Rubbia, *Neutrino Detectors for Future Experiments*, ETH Zurich (2004), arXiv:hep-ph/0412230v1

[48] A. Longhin, *Optimization of Neutrino Beams for Underground Sites in Europe*, Proc. Sci., ICHEP2010 (2012) 325, arXiv:1206.4294v1

[49] A. Longhin has kindly provided neutrino fluxes for the CN2PY experiment at *http://irfu.cea.fr/en/Phocea/Pisp/index.php?id=72*

[50] M. D. Messier, *Evidence for neutrino mass from observations of atmospheric neutrinos with Super-Kamiokande*, Doctoral thesis, Boston University (1999)

[51] E. A. Paschos and J. Y. Yu, *Neutrino interactions in oscillation experiments*, Phys. Rev. D65 (2002) 033002, arXiv:hep-ph/0107261

[52] A. M. Dziewonski and D. L. Anderson, *Preliminary Reference*

Earth Model, Phys. Earth Planet. Inter. 25, 297-356 (1981)

[53] E. Kozlovskaya, J. Peltoniemi and J. Sarkamo, *The density distribution in the Earth along the CERN-Pyhasalmi baseline and its effect on neutrino oscillations*, CUPP-7/2003 (2003), arXiv:hep-ph/0305042

[54] P. Coloma *et al.*, *Systematic uncertainties in long-baseline neutrino oscillations for large θ_{13}*, Phys. Rev. D87 (2013) 033004, arXiv:1209.5973v1

[55] S. Lorenz, *Discrimination of Neutral Current Background in a Future Long-Baseline Experiment with LENA*, Diploma thesis, Universität Hamburg (2012)

[55] R. Möllenberg *et al.*, *Reconstruction of GeV Neutrino Events in LENA*, AIP Conf. Proc. 1382, 141-143 (2011), doi:10.1063/1.3644294

[56] P. Huber, M. Mezzetto and T. Schwetz, *On the impact of systematical uncertainties for the CP violation measurement in superbeam experiments*, JHEP 0803 (2008) 021, arXiv:0711.2950v2

[57] S.S. Wilks, *The Large-Sample Distribution of the Likelihood Ratio for Testing Composite Hypotheses*, Ann. Math. Statist. 9, Vols. 60-62 (1938), doi:10.1214/aoms/1177732360

[58] X. Qian *et al.*, *Statistical Evaluation of Experimental Determinations of Neutrino Mass Hierarchy*, Phys.Rev. D86 (2012) 113011, arXiV:1210.3651

[59] E. Ciuffoli, J. Evslin and X. Zhang, *Sensitivity to the Neutrino Mass Hierarchy* (2013), arXiv:1305.5150v3

[60] J. Kopp, M. Lindner, T. Ota and J. Sato, *Nonstandard neutrino interactions in reactor and superbeam experiments*, Phys. Rev. D77, 013007 (2008), arXiv:0708.0152

[61] P. Huber and J. Kopp, *Two experiments for the price of one? The role of the second oscillation maximum in long baseline neutrino experiments*, JHEP 03 (2011) 013, arXiv:1010.3706

[62] P. Coloma and E. Fernández-Martínez, *Optimization of neutrino oscillation facilities for large θ_{13}*, JHEP 04 (2012) 089, arXiv:1110.4583

[63] S.K. Agarwalla, S. Prakash and S. Sankar, *Exploring the three flavor effects with future superbeams using liquid argon detectors* (2013), arXiv:1304.3251v1

[64] R. Petti and G. Zeller, *Nuclear effects in water vs. argon*, Tech. Rep. LBNE docdb No. 740

[65] J. Beringer *et al.*, Particle Data Group, PR D86 (2012) 010001, http://pdg.lbl.gov

[66] J.A. Formaggio and G.P. Zeller, *From eV to EeV: Neutrino Cross Sections Across Energy Scales*, Rev. Mod. Phys. 84 (2012) 1307, arXiv:1305.7513v1

[67] M. Blennow, *On the Bayesian approach to neutrino mass ordering* (2013), arXiv.org:1311.3183